Robotically 3D printed architectural membranes from ambient dried cellulose nanofibril-alginate hydrogel

Materials & Design 236 (2023) 112472

Contents lists available at ScienceDirect

Materials & Design

journal homepage: www.elsevier.com/locate/matdes

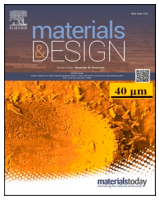

Robotically 3D printed architectural membranes from ambient dried cellulose nanofibril-alginate hydrogel

Malgorzata A. Zboinska [a,*], Sanna Sämfors [b,c], Paul Gatenholm [b,c]

[a] Department of Architecture and Civil Engineering, Chalmers University of Technology, SE-412 96 Gothenburg, Sweden
[b] Wallenberg Wood Science Center, Teknikringen 56–58, SE-100 44 Stockholm, Sweden
[c] Department of Chemistry and Chemical Engineering, Chalmers University of Technology, SE-412 96 Gothenburg, Sweden

ARTICLE INFO

Keywords:
Nanocellulose
Alginate
Hydrogel
Films
3D printing
Architectural design

ABSTRACT

Cellulose nanofibril hydrogel mixed with an aqueous solution of sodium alginate is a novel bio-based material suitable for 3D printing of lightweight membranes with exquisite properties and sustainable traits. However, fundamental knowledge enabling its applications in architectural design is still missing. Hence, this study examines the macro-scale features of lightweight membranes from cellulose nanofibril-alginate hydrogel, relevant for the design of various interior architectural products, such as wall claddings, ceiling tiles, room partitions, tapestries, and window screens. Through iterative prototyping experiments involving robotic 3D printing of lightweight membranes, their upscaling potential is demonstrated. Correlations between toolpath designs and shrinkages are also characterized, alongside an in-depth analysis of coloration changes upon ambient drying. Further, the tunability potential of various architectural features, enabled by bespoke 3D printing toolpath design, is discussed and exemplified. The aim is to expose the wide palette of design possibilities for cellulose nanofibril-alginate membranes, encompassing variations in curvature, porosity, translucency, texture, patterning, pliability, and feature sizes. The results comprise an important knowledge foundation for the design and manufacturing of custom lightweight architectural products from cellulose nanofibril-alginate hydrogel. These products could be applied in a variety of new bio-based, sustainable interior building systems, replacing environmentally harmful, fossil-based solutions.

1. Introduction

Materials play a pivotal role in shaping the built environment, constituting all buildings and structures. Where construction materials originate from and how they are manufactured has paramount importance for the environmental impact of any building. Yet, the building sector today consumes 50 % of the world's fossil resources, generates 40 % of global waste and causes 39 % of global carbon dioxide emissions [1]. Notably, the embedded carbon of building material production was proven to exceed the emissions of a building's operational phase [2]. In response to this realization, a profound shift in sustainability targets has occurred. Instead of only optimizing the building maintenance phases, the improvement of pre-construction phases is also a priority, focusing on more sustainable manufacturing of building components and materials. At the forefront of this important transition are the European Union policies, such as the *European Green Deal* that sets a benchmark of 49 % of renewable materials in buildings by the year 2030 [3]. A noteworthy example is also the *New European Bauhaus* funding initiative, supporting architectural design research on bio-based materials [4]. Beyond the EU endeavors, the Circular Economy (CE) approach is today established across various industry sectors. Its aim is to reduce resource consumption and waste generation by relying on side stream product upcycling and repurposing for new applications, as well as reuse of construction elements [5,6]. Nonetheless, many building materials today rely on fossil-based resources. To illustrate, the construction sector is still a prominent consumer of plastics, generating a notable 20 % of the total global demand for this material [7]. This is evident within building interiors, where plastics constitute a large share of the total material bulk [8]. Therefore, the significance of research on alternative materials that could reduce the environmental impact of buildings cannot be overstated, due to its direct effect on the sustainability of the built environment.

In response to the elevated demand for eco-friendly alternatives, a new research front has emerged, targeting novel materials from

* Corresponding author.
E-mail address: malgorzata.zboinska@chalmers.se (M.A. Zboinska).

https://doi.org/10.1016/j.matdes.2023.112472
Received 2 June 2023; Received in revised form 3 November 2023; Accepted 8 November 2023
Available online 10 November 2023

biomass. These materials contribute to circular economy as they originate from industrial side streams instead of depleting existing resources. The key constituents of these novel materials are all found in biomass, and include cellulose, starch, alginate, chitin, chitosan, and gelatin [9,10]. Cellulose, in particular, is coined as the most abundant one, as it prevails in byproducts of the world's largest industries, i.e., agriculture, marine farming, food manufacturing, forestry and paper production [11]. A paramount feature of cellulose is that its chains can be isolated as nanoparticles, which can, in turn, be used to build up a new group of bio-based nanomaterials referred to as nanocelluloses. The significance of nanocelluloses resides in their original properties, differing from those found in molecular cellulose and wood pulp [12,13]. Among these unique features, large surface area per unit mass, high tensile strength and high stiffness stand out [14–16]. Another robust property is the capacity of formulation with water and other bio-based ingredients into hydrogel suspensions. These hydrogels possess a valuable feature of shear thinning, enabling 3D printing applications [17–19]. Furthermore, they can be dried to derive strong nanocellulose membranes [20].

To put these versatile properties of nanocellulose into practical use, a large research front on its applications has emerged. For instance, studies targeting the biomedical industry have shown that nanocellulose hydrogels, due to their form stability, wetness and biocompatibility can act as 3D printed scaffolds for tissue and cell growth, and as wound dressings [21,22]. The electroconductive properties of dried films from nanocellulose have led to new applications as conductive paper, supercapacitors, and solar cells [23–25]. The supreme tensile strength of some nanocelluloses, matching that of Kevlar, has raised interest in military applications [26,27]. The same tensile strength, together with translucency, outstanding barrier properties against oxygen and air, and reasonable barrier properties to water vapor have led to their use in packaging solutions [28–30]. Another nanocellulose feature combination, i.e., its ability to form strong and gas-impermeable coatings, prompted its use in conservation of artwork and degraded construction timber, to protect from disintegration and deterioration [31–33]. The authors have investigated its use in architectural renovation, as a 3D printed decorative and protective coating for existing wooden interior panels [34]. Altogether, these unique attributes of nanocellulose do not only make it outstanding in the realm of advanced materials. They are also pivotal for its establishment as a bio-based alternative in less sustainable material systems, such as those relying on plastics, to reduce their environmental impact. Hence, new research effort is needed to enable applications of nanocellulose in architecture, in this way supporting the global efforts toward more circular design and construction.

The above overview shows that the properties of nanocellulose are robust enough to be suitable for architectural applications. Yet, a knowledge gap exists regarding such applications. Apart from the few studies exploring its use as coatings for timber, referred to above, a broader incorporation of nanocellulose in building components remains uncharted. A second, related knowledge gap concerns the material's characteristics established thus far. These characteristics do not cover the design features of nanocellulose. Instead, the focus has been on the functional features of the material, such as rheology for 3D printability, mechanical strength, electroconductivity and oxygen barrier properties, as well as its environmental performance parameters, such as biodegradability and recycling possibilities [30,35]. While fundamental from an architectural application perspective, these features do not represent a complete set of attributes of nanocellulose that would motivate its application as an architectural material. Deeper insight is needed on new design possibilities and aesthetic features of nanocellulose, demonstrating its applicability as a viable bio-based replacement within existing building systems. This so far missing focus with an architectural design outlook carries immense potential for not only knowledge advancement but also wide-reaching impact on near-future applications in various industry sectors. For building components and other consumer products, it can inspire smarter material choices and support new practices of bio-based, circular design.

Alongside the research advances in novel bio-based materials, studies targeting how these materials can be sustainably manufactured into specific products are also essential. One important manufacturing technique coined in this context is 3D printing, due to its outstanding environmental friendliness. Its benefits include the reduction of material waste by eliminating formwork [36], minimization of production time and human labor costs [37] and decrease in energy expenditures by over 70 % compared with other manufacturing methods [38]. Further, the superiority of 3D printing in the customization of the design and appearance of manufactured products is repeatedly highlighted. The ability to create individualized pieces, with virtually endless possibilities for aesthetic and geometric variation while not increasing the production costs entails important implications for the design of numerous products. It can fulfil the consumer need for product personalization, support manufacturer economy and satisfy the requirements for sustainable production [39–41].

Given these benefits, 3D printing has now permeated into the realm of bio-based material manufacturing. Several studies have already reported on 3D printing applications of bio-based hydrogels and paste-based biopolymer mixes for architectural and other design applications [42]. For instance, a hydrogel mix containing methylcellulose, sodium alginate and kappa-carrageenan was used to robotically 3D print an architectural panel prototype, laden with live algae cells for urban bioremediation purposes [43]. Hydrogels featuring blends of chitosan and sodium alginate were studied for applications in biodegradable architectural systems, yielding examples of functionally graded material constructs with varying mechanical properties and designs featuring material drying guidance [44–46]. Silk-based hydrogel formulations, 3D printed into leather-like sheets were investigated for textile industry applications, providing a characterization of material features that can be derived using intricate material recipes, and showcasing 3D printing pattern designs with strong architectural connotations [47].

Importantly, however, the current state of the art indicates that for 3D printing of hydrogel blends featuring nanocellulose and alginate in particular, the know-how is limited to the production of miniature objects only [19,21,22,48,49]. This points at an important knowledge gap concerning scalability—a crucial parameter for architectural applications due to products having larger dimensions. Another significant knowledge deficit concerns the 3D printing methods for hydrogels. Specifically, how the printing paths for material deposition are created. The present methods rely on path generation through automated 3D model slicing, and layer-by-layer material deposition. Custom design of the 3D printing paths, featuring tunable geometric design options and custom deposition patterns remains unexplored. A related issue is that the 3D printed products from nanocellulose hydrogels reported in previous studies were in the form of compact, solid pieces and not sheets, and they were not meant to be dried but rather remain in a wet state.

Furthermore, for dried products encompassing nanocellulose membranes, 3D printing as a production technique has not been studied. Instead, other methods, including vacuum filtration, casting evaporation, spray deposition and solvent casting were investigated. The latter two are now employed on a larger scale within the nano-paper industry [50–52]. Among these techniques, life cycle assessment studies have coined spray deposition as having the lowest environmental impact [53]. At the same time, the technique has limitations in terms of intricate designs. Only uniform nano-papers can be produced, and custom patterns cannot be achieved [54,55].

In addition to material deposition, the production of sheets from nanocellulose hydrogels requires a postprocessing stage of drying. To date, various drying methods have been investigated and established in the production of nano-papers, such as air or oven drying, freeze drying, spray drying, and solvent exchange drying. Although these techniques offer good results in terms of final product quality and processing time, they introduce high energy expenditures and require specialized instrumentation, which poses challenges, especially for films with larger dimensions [52]. This suggests that alternative drying approaches

should be sought and more deeply studied, to mitigate the environmental impact of the currently established but less sustainable drying techniques. In fact, studies comparing various drying techniques for nanocellulose films have already suggested that ambient drying, although taking the longest time, offers the greatest energy savings and does not require highly specialized equipment, contributing to a lower total environmental impact of nanocellulose products [56]. Hence, it could be applicable in some manufacturing contexts, such as fabrication of custom products at a smaller production scale. Altogether, the above state of the art points at the importance of new studies that would explore the knowledge gaps concerning the 3D printing of large, custom-designed membranes from nanocellulose hydrogel, and their ambient drying. This will provide the missing insights on scalability, design tailoring possibilities, macro-scale features of the dried membrane constructs, and on the intricacies of ambient drying.

In summary, considering all knowledge gaps discussed above, this study explores an uncharted area of nanocellulose hydrogel applications in architectural design. For the first time, the material is probed for its ability to be scaled up, robotically 3D printed and ambient dried into lightweight membranes with tailored design features. Additionally, the study contributes the missing insights on the correlation between custom computational design of the material deposition paths for 3D printing and the macro-scale effects of shrinkage and deformation during ambient drying. In this respect, the missing quantitative and qualitative characterizations are provided, describing the changes in membrane dimensions, forms, and outlines—in relation to specific toolpath design features. Further, a characterization of color transformations occurring upon hydrogel drying is also provided as a new element. Finally, the implications for design are laid out for the first time, pertaining to membrane design tunability and possibilities of product customization. This is done through a comprehensive characterization of fundamental aesthetic and formal attributes of 3D printed nanocellulose membranes, pertaining to shape, porosity, translucency, coloration, texture, pattern feature size, and pliability.

The significance of this study resides in the provision of new fundamental knowledge on the design, 3D printing and scaleup of architectural membranes from nanocellulose hydrogel. This knowledge is essential for the adoption of this new material in buildings. Given that materials comprise all buildings, and buildings are omnipresent, a shift from fossil-based solutions to bio-based ones can profoundly mitigate the negative environmental effects of construction. The study of sustainable materials can spark further advances in the design and manufacturing of bio-based architectural elements. It also opens possibilities for material innovation in architectural design, synergizing the perspectives of design and material science, to establish nanocellulose as a novel bio-based and sustainable alternative for building interiors of the near future.

The implications of this study for design and architecture reside not only in the new knowledge that helps to advance from fossil-based to bio-based material systems. In addition, they can also help to move from standard off-the shelf building components to highly customizable bio-based products for buildings. These products, through their design tunability, can be tailored to meet functional and aesthetic user requirements. This, in turn, can contribute to increased user acceptance and elevated demand for such solutions in the built environment. Having the knowledge base established in the present study is the first step toward the development of specific architectural products from nanocellulose hydrogel. From this knowledge foundation, design workflows and manufacturing sequences can be further developed, to meet the performance criteria and market needs for specific architectural product categories.

2. Method

The research method was based on the conduct of systematic prototyping experiments, in which nanocellulose constructs were manufactured with a gradual increase in dimensions, using various 3D printing toolpath designs and material deposition strategies. For each prototyping series, the experiment protocol applied to fabricate the membranes embraced five main stages (Fig. 1a).

The detailed experimental procedure for construct prototyping commenced as follows. Firstly, for each construct, a digital file describing its geometric design through a parametric definition of its toolpath was prepared in software environments Rhinoceros 3D and Grasshopper. The point data describing the geometry of the toolpath, together with the 3D printing parameters was then compiled into the G-code format via Grasshopper, and output as.iso files for the RegenHU printer, and as.src files for the KUKA robot. Then, larger CNF-ALG mixture batches were prepared for the prototyping, based on material quantity estimates. The required material volumes were calculated by multiplying the total toolpath length for each model by nozzle diameter and deposed material strand width. Parts of the CNF-ALG batch were then distributed into separate syringes in desired quantities and subjected to pigmenting. The pigments were water-based, so they were added to the material blend via syringe injection. The pigment was spread within the material via manual mixing using two syringes joined with a Luer-to-Luer connector.

In the next step, the material was loaded into the deposition cartridges of the 3D printer, and the G-code files were uploaded onto the machine through the human–machine software interface of respectively the RegenHU printer and the KUKA robot. Next, the G-code files were executed, and each construct was 3D printed, one at a time, onto a silicone underlay. Once 3D printed, each construct was photographed in top view using a digital camera. Afterwards, each construct was lifted carefully together with its silicone underlay from the printer bed, placed on a plastic tray, and subjected to crosslinking with an aqueous calcium chloride solution. Two crosslinking methods were applied, bath immersion and spraying. Bath immersion was done by carefully pouring an aqueous crosslinking solution onto the tray until the entire model was immersed. The second approach, used for the larger models, was to sprinkle the constructs with the solution from a spray bottle. The crosslinking mist was applied in multiple passes, until all fragments of the construct were fully covered. After one hour, the bathed models were removed with their silicone underlays from the trays. For the models treated with the mist, the crosslinker was removed by carefully drawing it into syringes and drying the remains with an absorptive paper towel. Finally, the crosslinked constructs were ambient dried, in conditions specified in the next section. For some models, a silicone sheet was periodically placed on top, for periods ranging between one to 24 h, to mitigate the deformation and curling effects. During the drying, intermediate model states were documented in photographs, taken at regular time intervals, between one hour to several days, depending on the observed model state changes.

2.1. Materials and postprocessing

The studied material formulation was based on a blend of cellulose nanofibril (CNF) hydrogel and an aqueous sodium alginate (ALG) solution. The material formulation followed a protocol described elsewhere [57]. In this study, a rough-grade, low-charge, enzymatically pretreated 2.3 % w/w CNF hydrogel dispersion from RISE Bioeconomy (Sweden) was used. To improve the stabilization of the 3D printed constructs, G-rich sodium alginate powder with viscosity of 160 mPa·s from Nova Matrix (Norway) was dissolved in 3 % w/w in deionized water and added to the CNF hydrogel formula in 80:20 w/w ratio. Finally, water-based edible pigments from Oetker Group (Germany) were added to the material in three primary colors, i.e., red, blue, and yellow, in various ratios and combinations, to obtain custom-colored hydrogels.

The postprocessing of the 3D printed constructs encompassed two steps: crosslinking and ambient drying. Crosslinking by forming ionic bonds between the polymer chains of sodium alginate and calcium ions

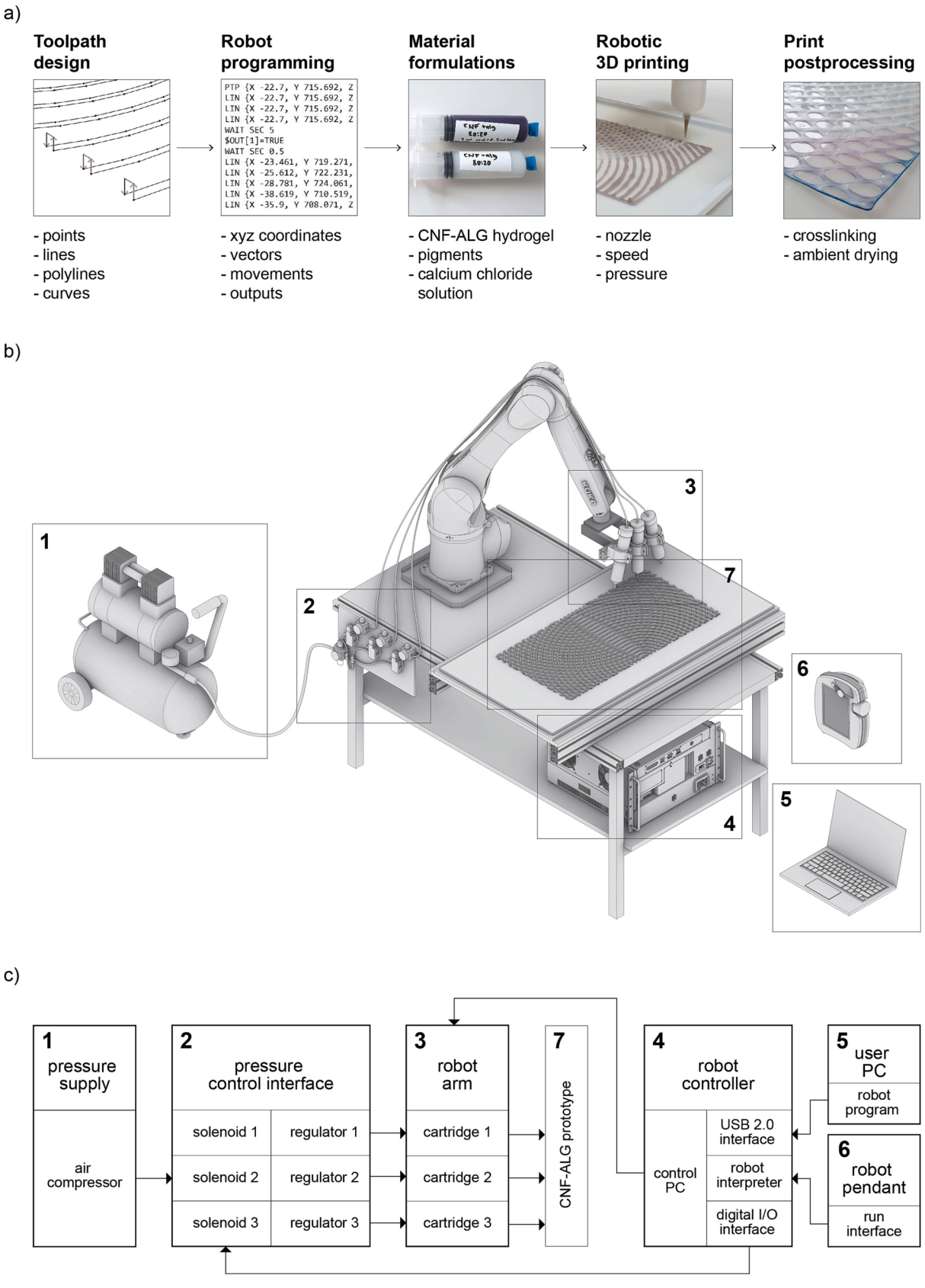

Fig. 1. A) Experiment protocol applied to fabricate the membranes, b) custom-designed robot cell setup for pressure-based extrusion, c) detailed scheme of interconnections between the mechatronic devices, hardware, and user interfaces for pressure-based extrusion within the robot cell.

was carried out by bathing and spraying the 3D printed constructs using a 2 % w/v aqueous calcium chloride solution. Ambient drying embraced placing a 3D printed and crosslinked construct on a non-stick, custom-cast silicone underlay at room temperature of 20 ± 2 °C and relative humidity of 30 % ± 2 %. For the smaller 3D printed constructs of the first experimentation series, the drying was done with no restrictions. For the larger constructs of the second experimentation series, the drying was conducted with restraint, i.e., a silicone sheet was placed on top of the constructs. The sheet was periodically taken away to enable water evaporation, and reapplied whenever significant deformations were observed.

2.2. Digital design and fabrication

The 3D printing experiments were conducted using two hardware systems. The first experiment series, focused on 3D printing of smaller constructs, was executed using a bioprinter RegenHU 3D Discovery with a workspace area of 9 cm × 13 cm. Standard, plastic, 10 ml dispensing syringes with a drip preventing Luer lock, plastic plungers, and dispensing tips with diameters of 0.85 mm and 1.2 mm were used to deposit the material at a constant pressure of 0.5 bar, provided from an air compressor.

The larger constructs were fabricated using an in-house, custom-built, pressure-actuated hydrogel extrusion system, deployed on an industrial robot KUKA AGILUS KR10 R1100 sixx with a working envelope of 813 mm × 971 mm. The fabrication work cell included a robot arm fastened to a table, and a printing bed mounted on top of the table using aluminum profiles (Fig. 1b). The mechanical assembly of the robot's end-effector for hydrogel extrusion comprised three interchangeable, 200 ml and 300 ml polypropylene cartridges with drip-free Luer locks, polyethylene plungers and exchangeable dispensing tips with diameters 0.85 mm, 1.2 mm, and 1.55 mm. The cartridges were mounted onto the robot's flange using an aluminum support frame and a custom, 3D printed clamping system. To enable multi-nozzle extrusion, the two side clamps for the cartridges were angled at 15 degrees in relation to the central axis of the robot flange, while the middle cartridge was aligned with the main axis. The pressure system enabling to deposit the hydrogel from the cartridges had three sub-components: the main compressed air supply, pneumatic precision regulators SMC G 1/4 0.01 MPa to 0.8 MPa for local pressure control, and pilot-operated, normally closed 3/2 RS PRO solenoid valves for pressure actuation (Fig. 1c). The pressured air was distributed to the cartridges from the main supply via the local regulator and actuation system through polypropylene pipes with a diameter of 6 mm. The solenoids were opened using 24 V electric signals. These signals were sent from the robot controller via digital outputs in a Beckhoff coupler module, according to programmed instructions that specified the initiation and termination of extrusion at desired locations and at scheduled time intervals.

The machine toolpaths and programs for both the RegenHU 3D printer and the custom-developed robotic extrusion system were generated via a parametric visual programming environment Grasshopper v. 1.0.0007 and custom coding modules programmed in Python. A free-form 3D modeling software Rhinoceros 3D v. 7.0 served as an interface for toolpath visualization. The RegenHU G-code generation was done directly from Grasshopper using Python code modules outputting an.iso file. The robot program was created using a Grasshopper add-in KUKA|prc v. 09.10.2022, which generated the robot code from toolpath data into an.src file in the KRL language native to the KUKA robot.

2.3. Experimentation framework and data acquisition

In the first experimentation series, twelve basic 3D printing experiments were carried out by 3D printing, crosslinking, and ambient drying small constructs with maximum dimensions of 30 mm × 40 mm. These trials were iterative and featured material deposition with gradually increasing toolpath complexity, ranging from basic linear and polylinear paths producing solid surfaces, to complex curvilinear paths generating non-uniform lattices. The analytical findings from these basic experiments, reported in Fig. 2, Fig. 3, Tables 1 and 2, have led to the identification of two 3D printing scenarios for the later production of upscaled constructs—solid and lattice deposition. The findings from this series also allowed to establish the starting parameter ranges for the upscaling experiments of series two, i.e., the number of layers, horizontal path offset, path elevation above the printing bed, printing speed, air pressure, and nozzle diameters. Analytical observations of ambient drying in the first experimentation series, featuring drying with no restrictions, have also enabled to preliminarily identify the construct deformation patterns, qualify the shrinkage levels, and understand the influence of various toolpath designs on the observed drying phenomena (Fig. 2, Fig. 3).

The deposition scenarios, 3D printing process parameters and membrane deformations identified in the basic trials of the first experimentation series have led to the definition of a systematic framework for the upscaling experiments of the second series. The experiments featured six different toolpath designs and material deposition strategies (Fig. 4), as well as sets of individually defined 3D printing parameters (Table 3). The toolpath designs and deposition strategies featured various complexity levels, from simple deposition using linear and polylinear paths, through more complex injection patterns and layered application of details achieved with pointillistic, linear, polylinear, and curved toolpaths, up to custom symmetric and asymmetric deposition using linear and curved toolpaths. As a result, six rectangular membranes with increasing dimensions were 3D printed, crosslinked and ambient dried (Fig. 5). During ambient drying, a restrictive silicone sheet was added on top of the drying constructs to observe its influence on the construct deformation trends.

The data specifying the dimension and outline changes occurring after 3D printing and ambient drying of these larger constructs was acquired through digital measurements in the Adobe Photoshop software using photographic data. This allowed for the acquisition of comparative data without causing damage to the wet constructs. For this purpose, all constructs were photographed at regular time intervals in top view using a digital camera Samsung Galaxy 9+, with lens parameters of 12 MP, f/1.5–2.4, 26 mm, 1/2.55 in, 1.4 μm, dual pixel phase detection autofocus (PDAF), and optical image stabilization (OIS). In the Adobe Photoshop v. 23.3 software, the photographs of the constructs in wet and dry states were resized with no digital compression to match the physical dimensions. Then, the width and length values of the outer maximum rectangular bounding envelopes were measured digitally. The average model shrinkages were then calculated using Eq. (1)

$$S = (OS - FS)/OS \tag{1}$$

where S is the shrinkage percentage (%), OS is the original wet model dimension and FS is the final dimension after drying and shrinking.

The outline changes for all constructs were analyzed through graphical vector-based tracing of outer object bounds in the Adobe Illustrator v. 27.4.1 software. The digital analyses of dimensions and shape transformations, together with the underlying data, are reported in Fig. 5, Fig. 6, and Table 4.

To characterize the color changes affecting the appearance of the final constructs, digital analyses of color saturation values were carried out. The numerical color saturation values were measured in the Adobe Photoshop v. 23.3 software, using the HSB (hue, saturation, and brightness) color model as a scale of reference. This model most accurately matches the human perception of colors [58]. For each studied construct, the HSB values were sampled from its photograph at three characteristic points. The registered values were collected for construct photographs in both the wet and dried state to allow for comparisons. The resultant color saturation changes and underlying data are reported in Fig. 6 and Table 3.

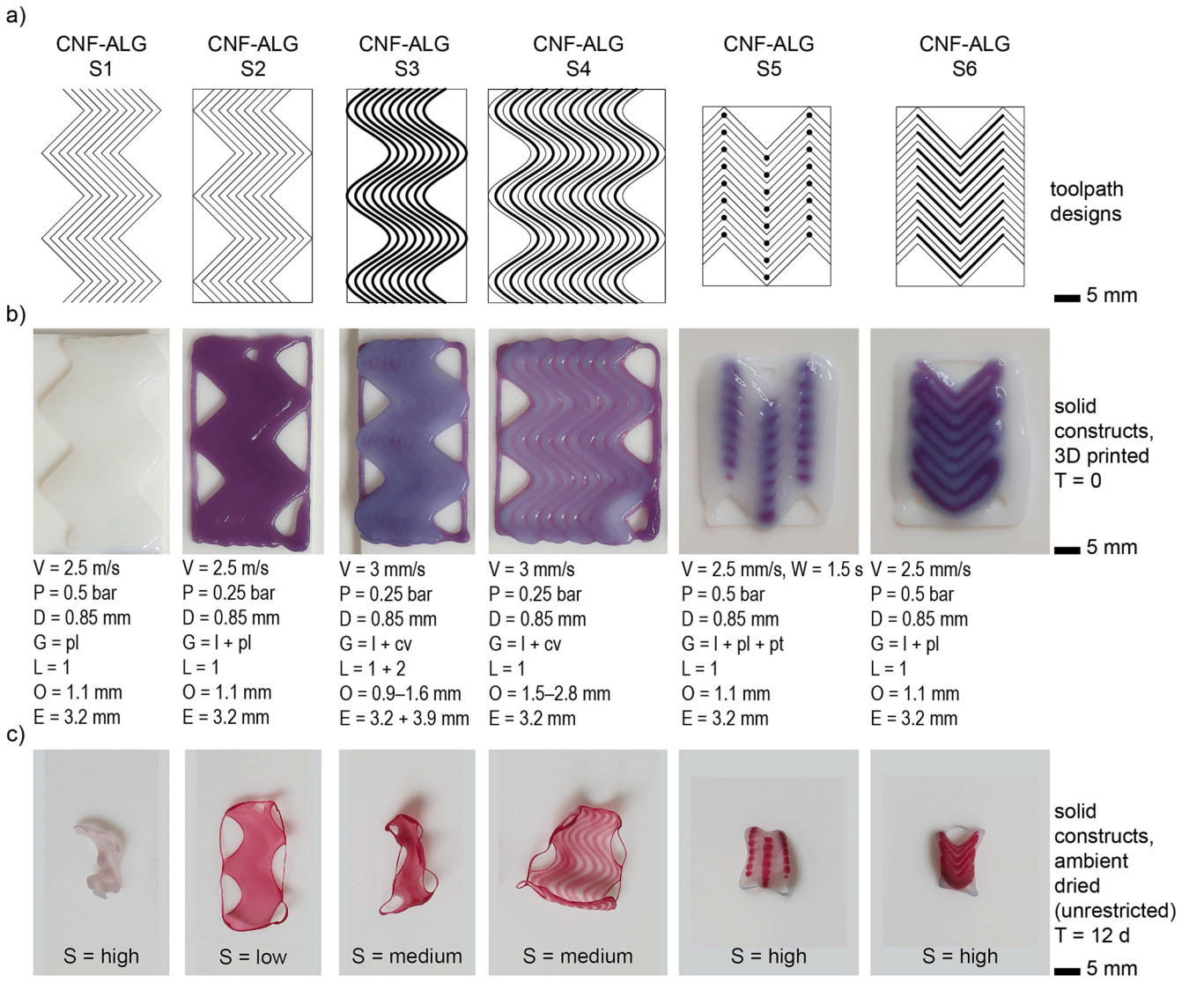

Fig. 2. Results of experimental prototyping of solid constructs in the first experiment series, with a specification of toolpath design and 3D printing parameters: printing speed (V), air pressure (P), nozzle diameter (D), toolpath geometry (G) featuring linear (l), polylinear (pl), curvilinear (cv) and pointillistic (pt) paths, number of layers (L), horizontal offset between the paths (O) and path elevation above printer bed (E). a) Toolpath designs employed to fabricate the respective constructs, b) photographs of constructs in wet state directly after 3D printing, c) photographs of constructs in dry state 12 days after ambient drying with no restriction.

In the last step of the investigation, the final characterizations of tunable membrane features in relation to the 3D printing parameters were derived based on analyses of video-photographic documentation capturing the 3D printing, crosslinking, and ambient drying of each construct at regular time intervals. The results of the analyses and tunable feature characterizations are reported in Fig. 8 and discussed in detail in the next section.

3. Results and discussion

3.1. Shrinkage and outline deformations

In the first experimentation series, two methods of material deposition were investigated: solid deposition and lattice deposition, with Fig. 2 and Fig. 3 reporting on the dimensional changes, deformations, and shrinkage. Tables 1 and 2 present the results of construct measurements, carried out for the wet and ambient dried states.

For the six constructs 3D printed using solid deposition, three (Fig. 2, CNF-ALG S1, S5 and S6) exhibited the highest shrinkage along their height, with the maximum value of 65 %. These constructs were 3D printed based on two different toolpath designs. One (Fig. 2, CNF-ALG S1) was manufactured with one polylinear layer and no rim, whereas the other two (Fig. 2, CNF-ALG S5, S6) were printed also in one layer, yet they additionally featured pointillistic and polylinear material injections. Both toolpath designs, together with higher extrusion pressure values of 0.5 bar, have resulted in large construct thicknesses. This has likely caused high shrinkage due to a large volume of water needing to evaporate in relation to a small surface area of the models.

Two constructs exhibited medium shrinkage along their height, 50 % and 53 % (Fig. 2, CNF-ALG S3 and S4). These constructs featured a rectangular rim toolpath, and, respectively, two curvilinear toolpath layers (Fig. 2, CNF-ALG S3), and one curvilinear layer deposited in two manufacturing passes (Fig. 2, CNF-ALG S4). Both toolpaths, together with lower extrusion pressure values, have yielded lower thicknesses of the constructs. Together with the presence of a form-stabilizing rectangular rim and partial adhesion to the printer bed, this has likely contributed to their lessened shrinkage.

One construct (Fig. 2, CNF-ALG S2) had a significantly lower

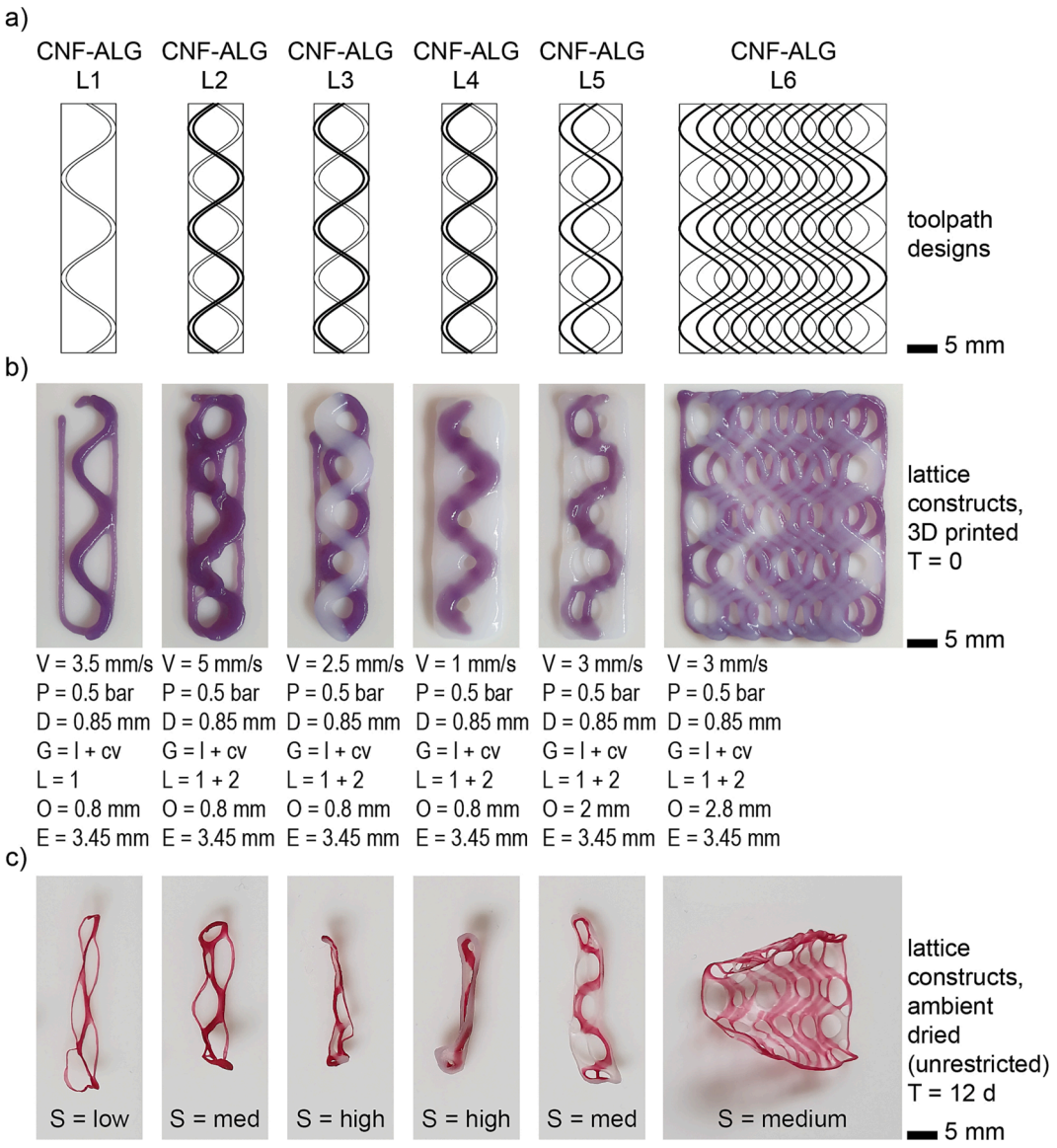

Fig. 3. Results of experimental prototyping of lattice constructs in the first experiment series, with a specification of toolpath design and 3D printing parameters: printing speed (V), air pressure (P), nozzle diameter (D), toolpath geometry (G) featuring linear (l), polylinear (pl), curvilinear (cv) and pointillistic (pt) paths, number of layers (L), horizontal offset between the paths (O) and path elevation above printer bed (E). a) Toolpath designs employed to fabricate the respective constructs, b) photographs of constructs in wet state directly after 3D printing, c) photographs of constructs in dry state 12 days after ambient drying with no restriction.

Table 1
Dimensions and shrinkage values for the 3D printed and ambient dried solid constructs in the first experiment series.

Prototype	State	Height (mm)	Height shrinkage (%)	Qualitative shrinkage rating
CNF-ALG S1	wet	40	65	high
	dry	14		
CNF-ALG S2	wet	40	38	low
	dry	25		
CNF-ALG S3	wet	40	53	medium
	dry	19		
CNF-ALG S4	wet	40	50	medium
	dry	20		
CNF-ALG S5	wet	34	62	high
	dry	13		
CNF-ALG S6	wet	34	62	high
	dry	13		

Table 2
Dimensions and shrinkage values for the 3D printed and ambient dried lattice constructs in the first experiment series.

Prototype	State	Height (mm)	Height shrinkage (%)	Qualitative shrinkage rating
CNF-ALG L1	wet	40	28	low
	dry	29		
CNF-ALG L2	wet	40	38	medium
	dry	25		
CNF-ALG L3	wet	40	48	high
	dry	21		
CNF-ALG L4	wet	40	45	high
	dry	22		
CNF-ALG L5	wet	40	33	low
	dry	27		
CNF-ALG L6	wet	40	40	medium
	dry	24		

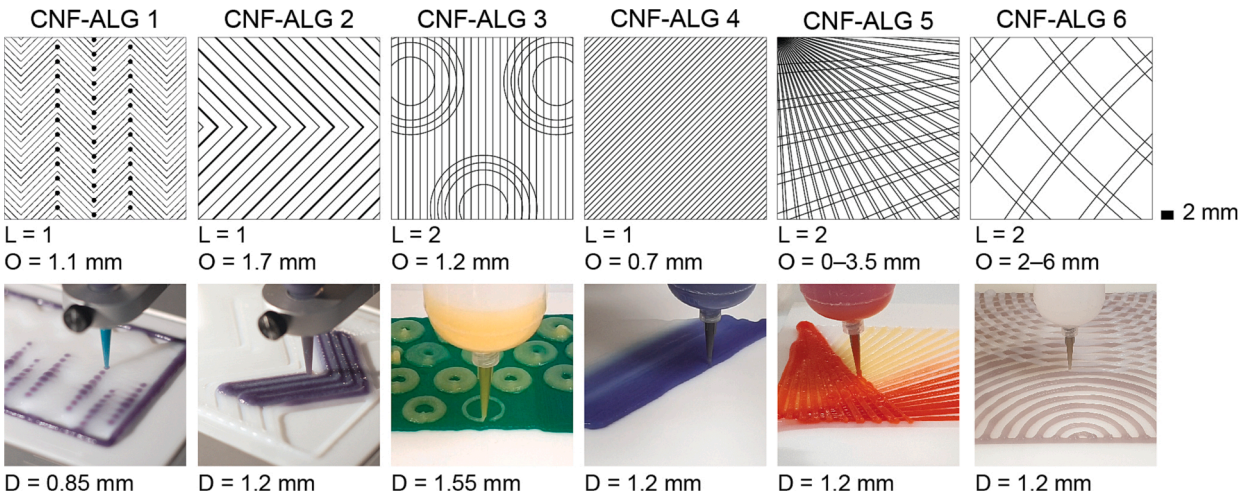

Fig. 4. Six toolpath designs and some of the characteristic 3D printing parameters applied in the second experiment series: number of layers (L), horizontal offset between the paths (O) and nozzle diameter (D).

Table 3
3D printing parameters in the fabrication of constructs in the second experiment series.

Prototype	Deposition strategy	Toolpath bounds (W × L mm)	Path offset (mm)	Path elevation (mm)	No of layers	Nozzle diameter (mm)	Printing speed (m/s)	Extrusion pressure (bar)	Extrusion tool
CNF-ALG 1	Solid, polylinear, point injections	62 × 88	1.1	2	1	0.85	0.005	0.50	RegenHU 3D Discovery
CNF-ALG 2	Solid, polylinear, line injections	72 × 100	1.7	2	1	1.2	0.005	0.50	RegenHU 3D Discovery
CNF-ALG 3	Solid, linear orthogonal, circular pattern	90 × 186	1.2	3 (base) 5 (pattern)	2	1.55	0.005	0.25–0.35	KUKA Agilus KR10
CNF-ALG 4	Solid, linear diagonal	90 × 200	0.7	2	1	1.2	0.005	0.35	KUKA Agilus KR10
CNF-ALG 5	Lattice, linear asymmetric	92 × 202	0–3.5	3 (base) 5 (top)	1–2	1.2	0.005	0.25	KUKA Agilus KR10
CNF-ALG 6	Lattice, circular symmetric	204 × 404	2–6	3 (base) 5 (top)	1–2	1.2	0.005	0.25	KUKA Agilus KR10

shrinkage value than others, namely 38 %. Its toolpath design featured a rectangular rim and an inner polylinear toolpath (Fig. 2, CNF-ALG S2). This construct had a low thickness value and a large area of adhesion to the silicone underlay, likely induced by the sharper corners of the toolpath compared with the curvilinear counterparts which exhibited a weaker tendency to adhere. These factors were the probable causes of the lowest shrinkage value.

The general conclusion from this set of experiments is that tightly packed material strands caused by small horizontal toolpath offsets, multiple toolpath overlays and material injections may yield large final thickness of the constructs. In combination with high extrusion pressure values and a low surface area, this may induce high shrinkage values. Further, it can be stated that the presence of a rectangular rim of material around a construct with an inner toolpath featuring a freeform design can have, to a limited extent, a stabilizing effect mitigating shrinkage and deformation. Another observation is that for solid deposition, the toolpath geometry featuring sharp instead of curved edges, e.g., a polylinear path instead of a curvilinear one, promotes better adhesion of the construct to the printer bed and hence limits the shrinkage effect.

For the six constructs 3D printed using lattice deposition, the highest shrinkage along the height, reaching 48 %, was noted for two (Fig. 3, CNF-ALG L3 and L4). It was likely caused by a combination of two toolpath design parameters, namely a small horizontal offset value between the paths (0.8 mm) and the number of paths (2). In addition, also by low speeds of deposition (1 mm/s and 2.5 mm/s). The resultant constructs had a large thickness and showcased bulky, nearly solid deposition effects. As already observed for the solid models, a large quantity of material deposited on a small surface area causes high shrinkage.

Medium shrinkage values, 40 % and 43 %, were recorded for two constructs (Fig. 3, CNF-ALG L2 and L6). These constructs featured two toolpath layers, deposited at higher speeds (3 mm/s and 5 mm/s), which yielded thinner material strands and high porosities of the models, contributing to the reduced shrinkage effect. The lowest shrinkage values, 28 % and 33 %, concerned the two remaining constructs (Fig. 3, CNF-ALG L1 and L4) and were likely correlating with the small width and height of the deposited material strands, a single layer for one of the constructs, and a large horizontal offset between the adjacent paths for the other construct (2 mm). Together with a large area of adhesion of these constructs to the printing bed, these factors have limited the shrinkage effect.

A summative conclusion from this set of experiments is that in lattice deposition, the larger strand width caused by small horizontal offset between the paths, and large layer height values caused by layered toolpaths can be correlated with higher shrinkage values. Therefore, lower shrinkage can be achieved through a combination of a highly porous toolpath design and 3D printing process parameter adjustments, such as a higher material deposition speed and lower pressure values, that altogether decrease the width and thickness of the material strands.

Collectively, the main findings from this first experimentation series were that models manufactured according to the lattice deposition strategy exhibited lower shrinkage values compared with the solid-deposited models. For both deposition types, small horizontal path

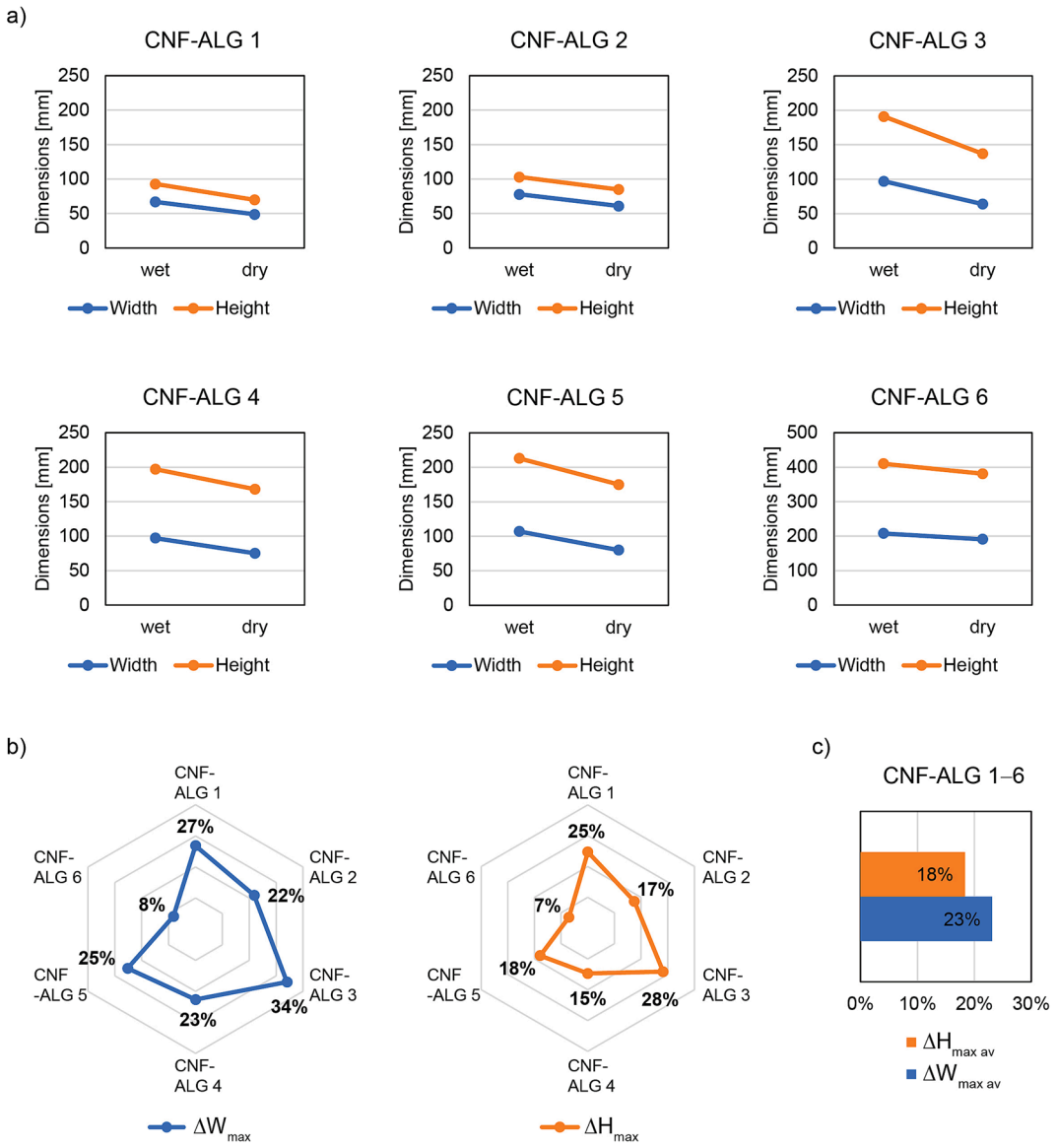

Fig. 5. A) dimensional changes upon ambient drying for width and height of the respective constructs, b) comparison between shrinkage values for width (w) and height (h) of the respective constructs, c) comparison between average shrinkage values for width (w) and height (h) of all constructs.

offset distances, combined with lower speeds of deposition, i.e., those less than and equal to 2.5 mm/s, yielded larger layer widths and heights, and hence higher shrinkage. This leads to an observation that shrinkage could be mitigated by increasing the printing speed in combination with an increased horizontal offset distance between the adjacent toolpaths, as well as by introducing a rectangular rim around the 3D printed pieces, and polylinear instead of a curvilinear toolpath design.

In the second experimentation series, to verify and extend the findings of the first experimentation round, both deposition methods, i.e., solid and lattice deposition, were further probed by designing toolpaths with different geometric features and levels of complexity. Fig. 4 shows the geometric features of these toolpath designs. Table 3 presents the specific toolpath design data and 3D printing parameters applied in the manufacturing of each construct. The constructs of this series featured gradual increase in dimensions, to assess scalability and compare the already observed shrinkage phenomena with those found in the larger constructs. For the ambient drying part of the process, in this experimentation series an additional sheet was placed on top of all constructs to further investigate the shrinkage mitigation possibilities.

Fig. 5 and Table 4 report the main findings regarding respectively shrinkage and dimensional data from measurements carried out for wet and ambient dried states. In terms of shrinkage along the width and height of the constructs, for five out of six constructs the shrinkage curves were close to parallel (Fig. 5a, CNF-ALG 1, 2, 4, 5 and 6), and one exhibited a more abrupt change in height in comparison with the change in width (Fig. 5a, CNF-ALG 3). In general, for all constructs, higher average shrinkage values were noted for the width compared with the height, with the differences ranging between 1 % and 8 % (Fig. 5b). On average, for all studied constructs, the maximum shrinkages for height were 18 % and for width 23 % (Fig. 5c), yielding a total shrinkage average of 20.5 %.

Fig. 6 illustrates the toolpath designs (Fig. 6a), resultant wet (Fig. 6c) and dry (Fig. 6d) constructs, as well as average shrinkage values and graphically represented changes in the outlines of the respective constructs (Fig. 6b). For these constructs, the highest average shrinkage of 31 % occurred in the one 3D printed using solid deposition and whose toolpath design featured local overlays of two material layers (Fig. 6, CNF-ALG 3). Even if these overlays were distributed and did not cover the entire surface of the construct, the shrinkage was nonetheless the highest. This confirms the observation from the first experiment series

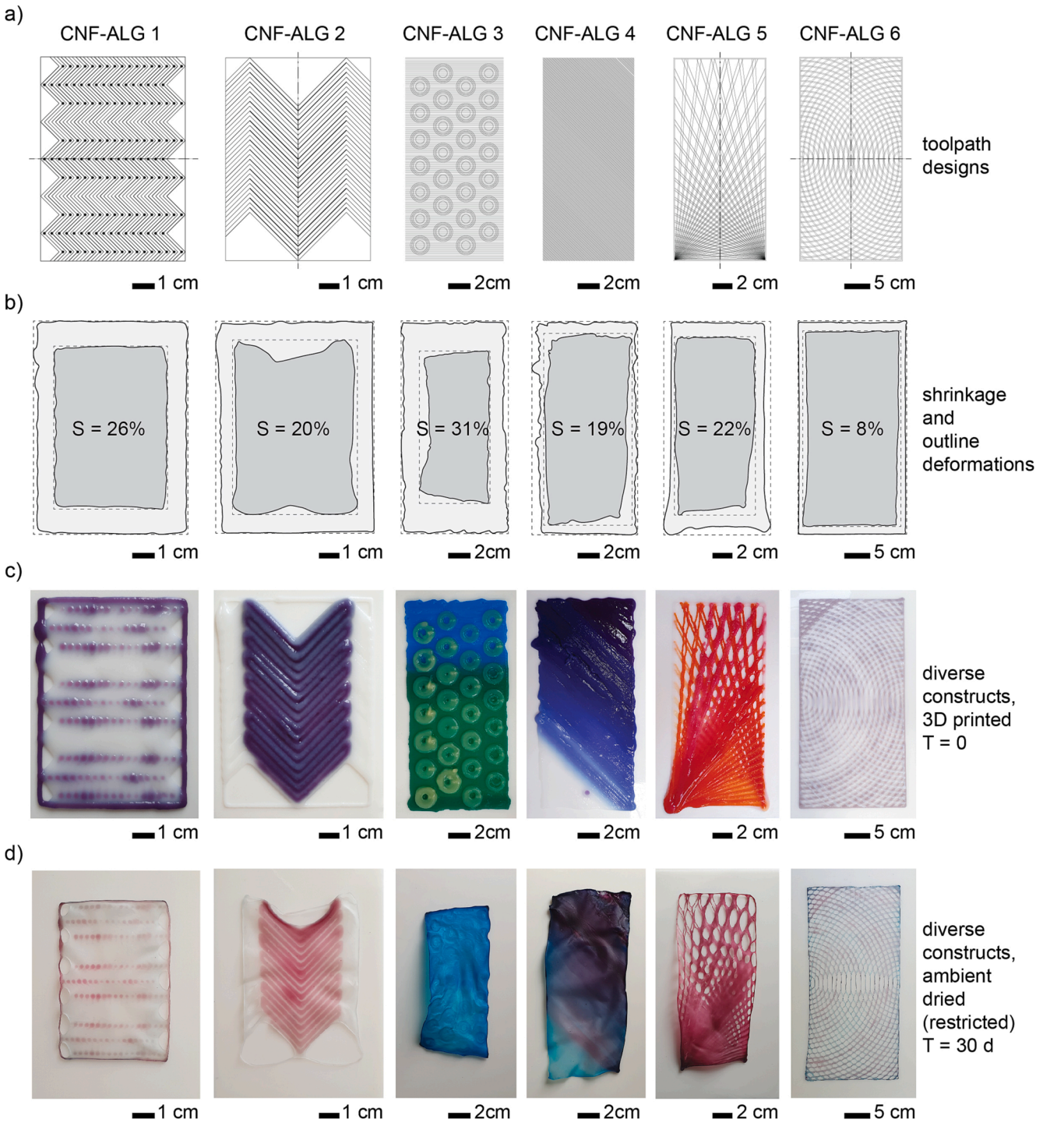

Fig. 6. Results of experimental prototyping of upscaled constructs in the second experiment series. a) Toolpath designs employed to fabricate the respective constructs, b) graphical analysis of outline changes from wet to dry state and the average shrinkage (S) values for the respective constructs, c) photographs of constructs in wet state directly after 3D printing, d) photographs of constructs in dry state 30 days after ambient drying with restriction using a flattening sheet.

that solid models with two or more layers, having large resultant thickness, exhibit higher shrinkage compared to models with only one layer and a low thickness. The lowest shrinkage value of 8 % was noted for the lattice-deposited model (Fig. 6, CNF-ALG 6), featuring high porosity and low layer width and height, confirming the inferences from the first experiment series concerning the potential of lattice deposition to yield lower shrinkages. The medium shrinkage values, varying between 19 % and 26 %, were noted for the remaining four constructs 3D printed according to both solid and lattice deposition methods (Fig. 6, CNF-ALG 1, 2, 4 and 5). Among these models, three featured solid deposition (Fig. 6, CNF-ALG 1, 2, 4) and one was 3D printed using lattice deposition (Fig. 6, CNF-ALG 5). Interestingly, the lattice construct did not have the lowest shrinkage value out of the four. Instead, the solid model featuring one layer exhibited the lowest shrinkage (Fig. 6, CNF-ALG 4). The unexpected higher shrinkage value of the lattice model was most likely caused by its asymmetrical toolpath design, featuring radial distribution of the paths. Specifically, this toolpath design resulted in locally high material accumulations in two model corners where

Table 4
Dimensions and shrinkage values for the 3D printed and ambient dried constructs in the second experiment series.

Prototype	State	Width (mm)	Height (mm)	Width shrinkage (%)	Height shrinkage (%)	Average shrinkage (%)
CNF-ALG 1	wet	67	93	27	25	26
	dry	49	70			
CNF-ALG 2	wet	78	103	22	17	20
	dry	61	85			
CNF-ALG 3	wet	97	191	34	28	31
	dry	64	137			
CNF-ALG 4	wet	97	197	23	15	19
	dry	75	168			
CNF-ALG 5	wet	107	213	25	18	22
	dry	80	175			
CNF-ALG 6	wet	208	410	8	7	8
	dry	191	381			

the origin points of the paths converged. This, in turn, has yielded an uneven total thickness of the construct, causing higher shrinkage of the part with the largest material quantity condensed per surface area, and the largest thickness. As can be observed in Fig. 6b and Fig. 6d, the other part of this construct featuring high porosity has shrunk less. Nonetheless, the total shrinkage value for the entire model has exceeded that of the uniformly deposited solid model (Fig. 6, CNF-ALG 4), in which the shrinkage occurred more uniformly and less abruptly due to the lower overall thickness of the construct.

In terms of outline deformations, the lowest deviations from the initial rectangular outer envelope are observed for two models, one manufactured using solid deposition and the other using lattice deposition (Fig. 6, CNF-ALG 1 and 6). Both constructs maintained their rectangular shapes after ambient drying. The lattice model was fully flat whereas in the solid one, low-level undulation occurred across the surface. For the solid model, the almost flat effect, not observed in any of the earlier experiments, was likely due to uniform material deposition and low model thickness, as well as the presence of symmetrically distributed porous features along two edges, which allowed the material to shrink and deform more uniformly. For the lattice model, the flatness can be attributed to the high level of porosity, low layer width and large distances between the deposited material strands, mitigating shrinkage. The same effect of maintaining flatness and outline stability was observed for the other lattice model in its upper part featuring high porosity (Fig. 6, CNF-ALG 5). The largest geometric deformation, characterized by non-uniform bending and large outline deviation occurred in the mostly shrunk model (Fig. 6, CNF-ALG 3). The non-uniform bending effect was likely induced by uneven material thickness and specific toolpath design of the secondary circular patterning layer. Specifically, as seen in Fig. 6d, the left part of the construct that underwent bending had solid circular material islands with larger thickness than the islands on the right part (Fig. 6c). This effect was not designed but rather occurred due to non-uniform material deposition, caused by variations in pressure due to the plunger becoming stranded in the cartridge, causing an air cushion to emerge between the material and the plunger. As a result of this uneven material distribution, the drying deformations were also uneven, leading to the already mentioned effects of non-uniform bending and asymmetrical outline deformation.

Another characteristic deformation effect was noted for the construct 3D printed using solid deposition, featuring a linear toolpath design with a diagonal orientation toward the outer model boundary (Fig. 6, CNF-ALG 4). As a result, this membrane exhibited a skewed deformation. This suggests that asymmetry in the toolpath design and material deposition will likely be reflected in the final dried constructs. On the contrary, if the toolpath orientation follows the main longitudinal and transversal axes of the main outline, the deformation will be uniform instead. This is confirmed by the effects in the constructs featuring zigzag polylinear toolpaths oriented in accordance with one of the main model axes (Fig. 6a, CNF-ALG 1 and 2). The symmetry also played a role in the lattice model with least deformation, where circular, mirrored toolpaths followed both central axes of the model, causing a uniform deformation effect (Fig. 6a, CNF-ALG 6).

In terms of the upscaling through gradual increase in the construct width and height, and the correlation between shrinkage values and model dimensions, no evident trends or anomalies were observed. The increasing model dimensions did not seem to affect the shrinkage values. In fact, the lattice model having the largest dimensions exhibited the lowest shrinkage. The other models of the series, despite their varying dimensions, exhibited higher yet less spread out shrinkage value ranges, between 19 % and 26 %. At the same time, the relationship between construct thickness and its outer dimensions is still an important factor affecting shrinkage, and it needs to be considered during upscaling. This can be inferred from the effects in the circular pattern and the asymmetric lattice constructs (Fig. 6, CNF-ALG 3 and 5), in which the varying thicknesses strongly influenced the deformation trends. The effects noted for the latter construct also indicate that there exists an evident correlation between the width of the material strand in the lattice model and its ability to remain flat. This relation is to be further characterized and quantified in future studies.

Finally, regarding the correlation between flatness and the ambient drying method featuring an overlay placed on top of the drying constructs, it can be concluded that the mitigation effect is most pronounced for constructs having a low total thickness and high porosity. The use of the drying overlay did not significantly mitigate the deformations in the three constructs exhibiting the highest deviations from the initial rectangular outline (Fig. 6, CNF-ALG 3, 4 and 5). These constructs had asymmetries in the toolpath design, and non-uniformities in material distribution and layer height, which can be linked to their larger deformations. The unequal material distribution and height of the constructs caused uneven water evaporation, with some zones drying and deforming faster and more abruptly, and others remaining wet for longer periods of time. On the other hand, the three constructs with the least deformations and that remained nearly flat had porosity features, symmetric toolpaths, and low layer height, as well as uniform material distribution (Fig. 6, CNF-ALG 1, 2 and 6). This, together with the use of the flattening sheet, allowed to equalize the water evaporation across their surfaces and mitigate large deformations.

The inferences from these analytical findings, pertaining to the correlation mechanism between toolpath design features, and shrinkage and deformations, converge into two conclusions. Firstly, solid material deposition, with tight spacing between the paths and featuring at least two layers, where at least one is asymmetrically distributed on top of the other, is responsible for large, uneven deformations and high level of shrinkage in the final dry constructs, above 30 %. Secondly, small deformations and low shrinkage values, below 10 %, can be achieved if the toolpath design is based on material strands forming a highly porous construct with a symmetric path layout. These two correlations are shown in Fig. 7.

3.2. Color saturation changes

Fig. 8 illustrates the color saturation changes investigated at various

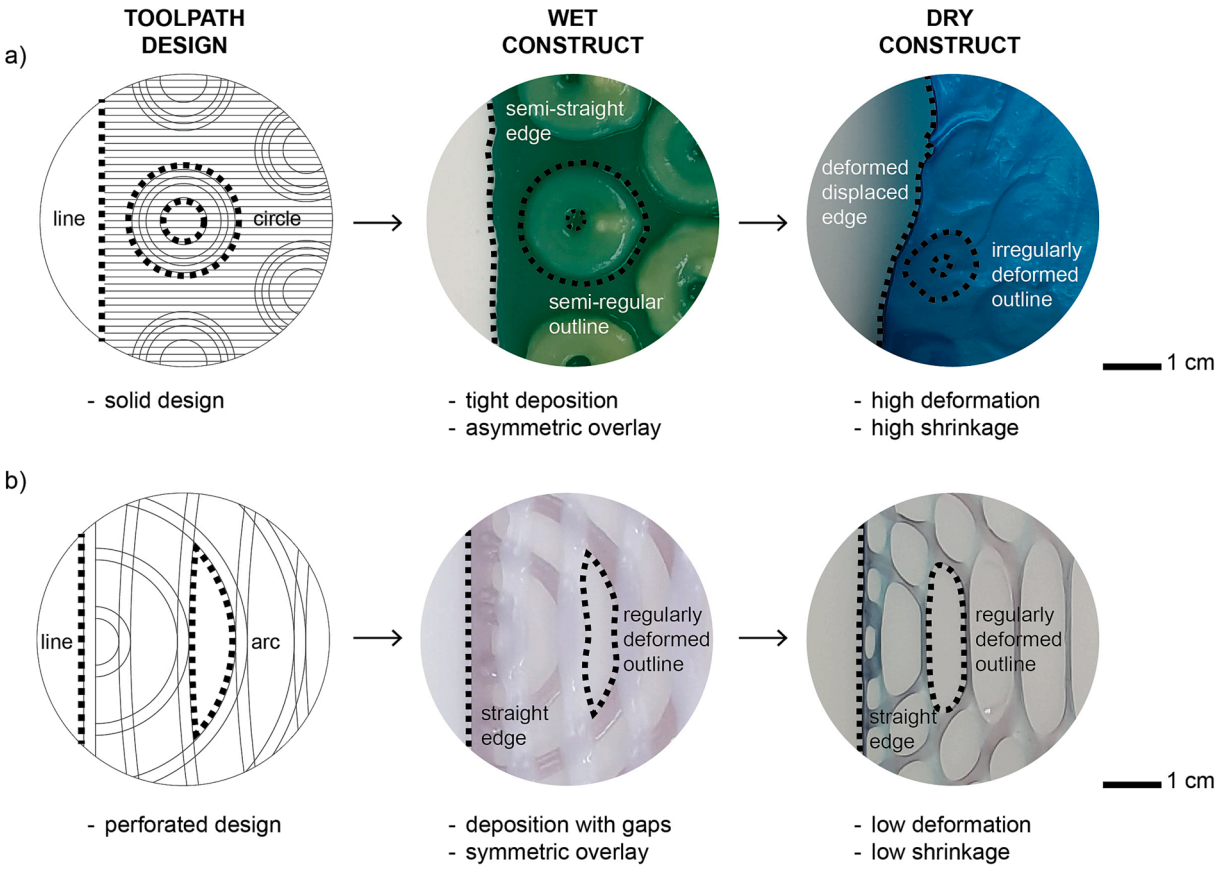

Fig. 7. Correlation mechanism between 3D printing path features, material deposition, and shrinkage and deformation effects in the final ambient dried constructs, shown in detail for a) the CNF-ALG 3 construct, representing the highest shrinkage and deformation, and b) the CNF-ALG 6 construct, representing the lowest shrinkage and deformation.

points located within the surfaces of selected models. The general conclusion concerning color transitions is that they can vary greatly, making it difficult to capture evident trends. This can be seen in Fig. 8, showing a large span and irregularities in the registered color saturation values for the studied constructs. However, it is still possible to conclude that color transitions for the studied models depended on three factors, namely the saturation of pigment per volume unit of the material, the crosslinking method, and solubility and color stability of the pigment used. Further, in case of color patterning, the material deposition strategy and toolpath design also played a major role in how the color distribution effects presented themselves in the final membranes.

The characteristics of color saturation changes observed for the 3D printed constructs are as follows. The construct manufactured from a material blend having a high concentration of blue pigment (Fig. 8b, CNF-ALG 3) exhibited notably increased saturation values after ambient drying. A large change in saturation values also occurred for those constructs in which cross-contamination with pigments dissolved in the crosslinking solution took place. This was the case for the initially white and non-pigmented parts of the CNF-ALG 5 construct at measurement point 1 (Fig. 8d), where the saturation increase was 64 % (Table 5), and due to contamination with red pigment. On the other hand, the constructs featuring lower concentrations of the red pigment, and mixed with the blue pigment to obtain a violet hue (CNF-ALG 2 in Fig. 8a and CNF-ALG 6 in Fig. 8e), have shown smaller variations in saturation, and a lower span of hue alterations. In four constructs (Fig. 8, CNF-ALG 1, 4, 5 and 6), the saturation was decreased for parts featuring non-stable pigments, i.e., yellow and blue, which became dissolved in the crosslinking solution, leading to color hue changes and color saturation losses in the final constructs.

The noted correlations between toolpath design, material deposition strategy, as well as color hue and saturation changes depended primarily on how the colored layers were deposited in relation to each other, in connection with the typical polymer network collapse phenomena accompanying water evaporation from the CNF-ALG hydrogel. From the results, it follows that discernible color patterns can be achieved either by introducing color gradients within the same 3D printed construct, as in CNF-ALG 3 (Fig. 8b), or by introducing color patterns via injecting extra material into an already 3D printed layer, as in CNF-ALG 2 (Fig. 8a). The use of color blends leads to seamless color transitions whereas injections allow to achieve clear-cut color patterns within the constructs.

On the other hand, patterned overlays of color through deposition of stacked material layers result in the colors blending with each other upon the collapse of the polymer network during CNF-ALG hydrogel drying. For monochromatic and primary colors, this leads to indiscernible color variations, due to the colors blending into hues close to each other on the color wheel. This is evident in construct CNF-ALG 4 (Fig. 8c), for which the initially yellow circular pattern overlay, when placed on a blue and green underlay, disappeared completely in terms of color variation in the final dry construct, yielding a uniformly distributed, monochromatic blue-green coloration. The pattern is visible only due to the higher concentration of cellulose fibers in the circular zones which were initially thicker, while the overall coloration of the construct is plain across its surface.

Finally, some of the color hue transitions are independent from the toolpath design strategy and instead correlated with the crosslinking method and pigment stability when exposed to contact with an aqueous crosslinking solution. If a mist is used to crosslink the construct, then cross-contamination of pigments and change of color hues is more notable, with some parts of the constructs becoming recolored

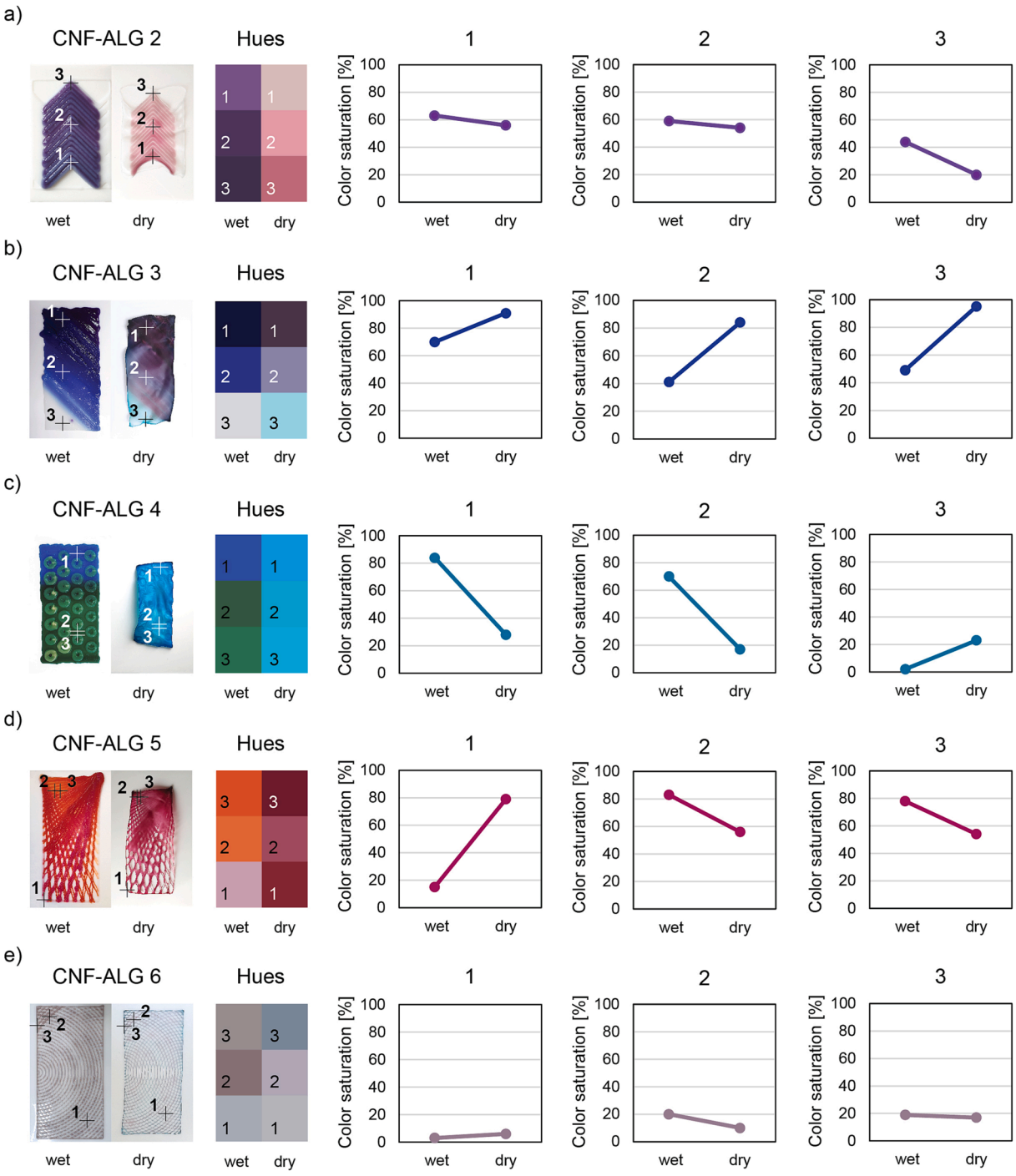

Fig. 8. A)–e) color hue and saturation changes registered at selected point locations (1–3) within the surfaces of the constructs, registered for wet and dry state.

significantly. This is seen in construct CNF-ALG 3 (Fig. 8b), in which the initially white and unpigmented corner became blue in the end. This was due to cross-contamination, i.e., transfer of blue pigment from the model parts with high pigment concentration into the crosslinking solution and absorption back into the material construct, across its whole surface. On the other hand, if full immersion of the construct in a crosslinking bath is used, the cross-contamination is usually less discernible whereas color loss is more evident for less stable pigments. This is seen in construct CNF-ALG 2, which initially featured a violet pattern obtained by blending red and blue pigments (Fig. 8a).

After immersion in the crosslinking bath, the blue portion of the pigment blend became dissolved in the bath, leaving the red pigment only.

3.3. *Adjustable membrane characteristics and their architectural relevance*

Fig. 9 illustrates adjustment ranges for seven characteristic CNF-ALG membrane features coined in this study, i.e., curvature, porosity, translucency, texture, feature size, patterning, and pliability. As discussed below, these characteristics can be modified using custom toolpath designs and specific 3D printing parameters. As such, they are relevant for the future application of CNF-ALG hydrogel in various architectural products.

Table 5
Color saturation values for the 3D printed and ambient dried constructs in the second experiment series.

Measurement point ID	State	Prototype				
		CNF-ALG 2	CNF-ALG 3	CNF-ALG 4	CNF-ALG 5	CNF-ALG 6
1	wet	63	70	84	15	3
	dry	56	91	28	79	6
2	wet	59	41	70	83	20
	dry	54	84	17	56	10
3	wet	44	49	2	78	19
	dry	20	95	23	54	17

Fig. 9a exemplifies the curvature modulation possibilities for the membranes, which span from producing fully flat through moderately undulant and up to strongly curved constructs. The curvature is controllable via toolpath design and material deposition strategy. Flat membranes can be obtained by applying the lattice deposition strategy, with toolpath designs required to have large offset distances between the respective paths. Hence, the flat membrane design is primarily limited to porous constructs, as the openings and apertures help to mitigate spatial deformations. If 3D printed using linear, polylinear, or curvilinear toolpaths featuring symmetry along both the longitudinal and transverse axes of the construct, and ambient dried with a flattening sheet, planar membranes are achievable. On the other hand, to manufacture nearly flat, moderately undulant membranes, solid material deposition can be applied as a 3D printing strategy. Linear, polylinear, and curved toolpath designs are applicable, keeping in mind that asymmetries in the toolpath design may cause distortions of the outer envelope of the construct upon drying. If planarity of the undulant membrane is desired, a low ratio between the deposited material thickness and the construct dimensions should be kept. Finally, strongly curved membranes can be obtained by varying the number of layers and therewith the thickness across the construct. The curvature is also achievable by applying a second thickening layer featuring an asymmetric layout. In general, to induce the bending effect upon membrane drying, the secondary and further layers of the toolpath can have any geometry. i.e., linear, polylinear, or curvilinear, but require at least two overlapping layers. More than one layer and large material thickness should be introduced in zones where formation of curvatures is to occur. The architectural relevance of curvature variation translates directly into high levels of geometric tunability of the membrane constructs. It entails that membranes with wide ranges of curvatures can be produced and applied in products requiring both flat and curved features, such as wall panels, standalone, free form suspended ceilings and claddings of rounded elements, such as circular pillars and curved walls.

Fig. 9b shows examples of porosity variations achievable in the CNF-ALG membranes. The openings can be tuned through toolpath design, to produce an infinite range of variously perforated constructs, from non-porous membranes, through elements having symmetrical and asymmetrical local openings, up to fully perforated, symmetrical, and asymmetrical net-like lattices. The offset distance between the toolpaths is the main parameter for tuning the porosity. The toolpath offset, together with the total width of the material strand, determines the level of porosity variation. In principle, all openings and apertures will exhibit curved shapes upon drying due to the fillet effect. Hence, linear, polylinear and curvilinear toolpaths can all be used to ultimately obtain rounded openings. As such, the tunable porosity, seen in the occurrence of apertures, openings, and perforations of the membranes, is relevant for a range of architectural products that require light and vision to pass through fully. These can include lightweight room dividers and wall partitions, window screens, skylights but also decorative elements, such as patterned wall tiles and suspended ceiling panels. Such elements can be assembled into versatile layered systems having functional and aesthetic roles. The multiple membrane layers can be designed to have varying porosities, with the size and location of apertures precisely controllable via the geometric design of the toolpath curves.

Fig. 9c exemplifies translucency variation possibilities in the membranes. Low-translucency membranes can be obtained through multi-layered toolpath design. To limit light and sight transmission, the extrusion nozzle diameter, offset distances between the respective paths as well as the elevation of the paths above the printer bed can be set to achieve tightly packed solid 3D deposition of the CNF-ALG material with a large resultant thickness. This will lead to a higher concentration of nanocellulose fibrils per unit area of the membrane, and opacity of the dried construct. On the contrary, translucent and transparent membranes can be achieved by designing single-layer toolpaths with larger in-between offsets and smaller elevation of the toolpath above the printer bed, resulting in a lower thickness and hence a smaller number of cellulose nanofibrils per surface area. In combination with a proper selection of either bright or dark pigments, the toolpath design can be an efficient tool for translucency tuning. Similar to porosity, the translucency variations have paramount importance in a wide range of architectural products that require control of light and vision transmission. Such products are space dividers and wall partitions for visual privacy, window shades, blinds for skylights as well as other interior furnishing components, assembled into versatile systems with variegated sight and light filtering functionalities.

As shown in Fig. 9d, CNF-ALG membranes can also exhibit a range of tunable textural features. The texture variations can be low, represented by flat and smooth finishes, as well as medium and high, with three-dimensional features such as ribs and grooves. The textures are tunable by synchronizing the toolpath elevation above the printer bed, horizontal offset between the paths, the number of layers and their geometric design. The higher the elevation above the printer bed and the larger the path offset distance, the rougher the surface finish, with toolpath traces visible within the membrane surface due to the deposed material accumulating into form-stable strands with strongly delineated boundaries. For ribbed effects, the layer number needs to be more than one, with the secondary layer acting as a patterned overlay on top of the first base layer. Textural effects are important to consider in the design of membranes that will be experienced at eye level and from a close distance, allowing to see and touch the texture. The textural features can also have a structural function, increasing the stiffness of the membrane construct. Examples of relevant architectural products include wall coverings and window screens, and all other elements in which textures have aesthetic and performative functions.

Fig. 9e exemplifies the pattern variation effects achievable in the CNF-ALG membranes. The main means for tuning the patterns is custom toolpath design featuring various geometric arrangements of toolpath curves and points. With this, toolpath design offers a limitless range of pattern variations. Through secondary toolpaths embedded within the base layer and material deposition based on injections, colored pointillistic and curved patterns of any shape can be obtained. The overlay of pattered layers, both lattice-like and solid ones, allows to obtain relief features within the membrane surface. Patterns with well delineated boundaries as well as those featuring gradient transitions can be achieved through combinations of material deposition paths based on points, lines, polylines, and curves. Overall, the patterning has similar architectural relevance as texture—it can act as an ornamental feature of the membrane, contributing to its aesthetic quality, as well as have a specific functional role, such as light transmission and translucency modulation, structural reinforcement, sound absorption or acoustic dispersion.

As shown in Fig. 9f, some membrane designs can also feature tunable pliability. This property concerns perforated membranes 3D printed using the lattice deposition strategy. A large enough distance between the paths forming the lattice is a paramount factor determining the ability of the membrane to flex. Furthermore, the direction and orientation of the toolpath curves in relation to the main axes of the construct will define the direction in which it will be able to bend. In general,

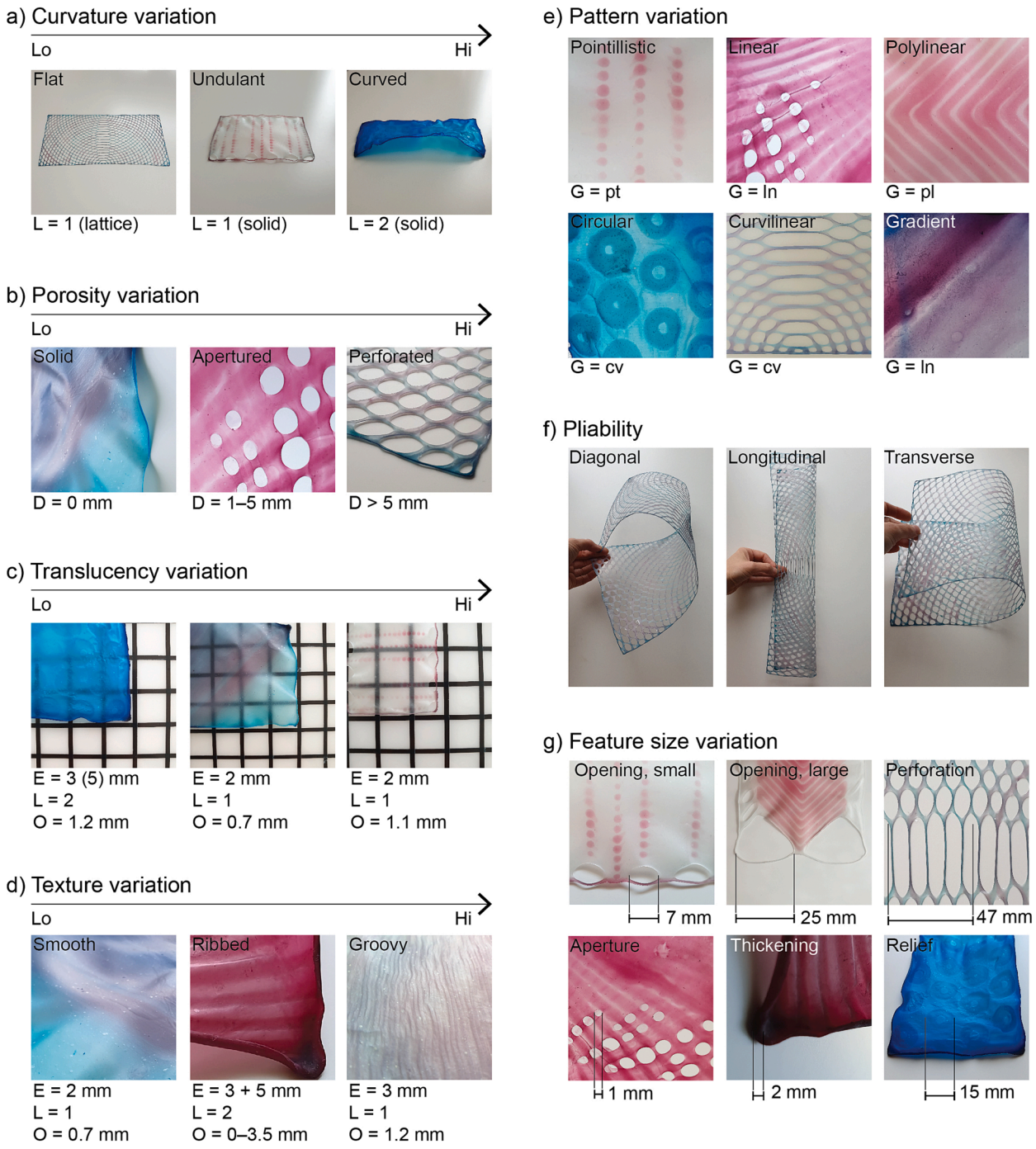

Fig. 9. Variation ranges from low (Lo) to high (Hi) for seven characteristic CNF-ALG membrane features: a) curvature, b) porosity, c) translucency, d) texture, e) pattern, f) pliability and g) feature size, with influencing parameters: nozzle diameter (D), toolpath geometry (G) featuring linear (l), polylinear (pl), curvilinear (cv) and pointillistic (pt) paths, number of layers (L), horizontal offset between the paths (O) and path elevation above printer bed (E).

toolpath designs symmetrical in relation to both the transversal and longitudinal axes of the construct will allow it to be flexed in these directions as well as diagonally. Pliability is an important feature for architectural elements that need to be mounted in-between existing interior components and adapt their form to an existing spatial setting. It is also important in mobile architectural systems, such as movable sunshades, window screens or reconfigurable room dividers that need to have a bending capacity.

Finally, Fig. 9g demonstrates the wide range of dimensional variations of the membrane features. The sizes of perforations, openings, apertures, structural reinforcements, and relief features can all be tuned through geometric toolpath design that can take virtually any desired pattern and shape. The feature dimensions in the prototypes ranged from 1 mm to nearly 50 mm, and the upscaling capacities shown through the experiments suggest that the maximum feature dimensions can be further increased to produce larger features in larger membranes. This feature size variability is relevant for the functional as well as aesthetic customization of multiple architectural membrane products intended for diverse applications, demonstrating high design versatility.

4. Conclusion and future work

The building sector requires urgent transition to more sustainable material systems that preserve the non-renewable resources and fully utilize the existing material flows. The hydrogel based on cellulosic and algal biomass can be derived from industrial side streams, presenting one such solution. It is renewable, biodegradable, structurally robust, and offers a wide range of tunable design features suitable for architectural applications in various lightweight building products, such as room dividers, window blinds, wall cladding panels, acoustic elements, and solar tiles. It is an advanced material solution with a significantly reduced carbon footprint, and for this reason deserves extensive studies to replace the environmentally harmful materials in buildings.

This study contributes to this dynamic research front investigating new applications of bio-based materials in buildings by focusing on the architecturally relevant traits of nanocellulose hydrogel. Through a knowledge crossover between architectural design and materials science, the following findings are provided. Firstly, fundamental architectural features of 3D printed, ambient-dried CNF-ALG membranes are coined, i.e., curvature, porosity, translucency, texture, color pattern, feature size and pliability. Design tunability and relevance of these features for various architectural applications are discussed. Secondly, the study demonstrates the scalability of CNF-ALG membranes achieved with the aid of robotic 3D printing technology, to match the dimensions of architectural products. The largest prototype is 200 mm × 400 mm and showcases further scale-up potentials. Thirdly, two main upscaling challenges are identified, i.e., shrinkage and deformation upon ambient drying. It is further discovered that these challenges can be mitigated through custom designs of the 3D printing paths. Fourthly, the 3D printed membrane shrinkage effects are quantified and correlated with specific design features of the 3D printing paths. The smallest outline deformation and lowest average shrinkage of 8 % is observed for fully perforated lattice membranes manufactured via material deposition along symmetrically distributed curvilinear paths. The largest outline deformation and highest average shrinkage of 31 % are noted for solid membranes fabricated via layered material deposition, featuring two solid layers and an asymmetric distribution of the uppermost deposition path. Lastly, it is demonstrated that the final color hue and saturation after crosslinking and ambient drying of the hydrogel membranes depend on toolpath design and the material deposition method, as well as on the physical and chemical properties of the pigments used. The most striking coloration changes embrace hue transitions due to pigment dissolution in the crosslinking liquid, and an increase in color saturation due to water evaporation during drying.

Considering these findings, the implications of this study for design include the identification of a wide range of 3D deposition strategies for the CNF-ALG material, and new insight on how these affect the final product appearance, dimensions, and form. This broadened understanding is important to develop a new generation of bio-based building products from nanocellulose, such as cladding, paneling and space divider systems. Owing to the knowledge foundations provided in this study, the designs of these products can be tailored to meet specific functional requirements and aesthetic user needs. The exquisite design customization potentials of the 3D printed CNF-ALG hydrogel can, in a long-term perspective, lead to an elevated demand for personalized products from bio-based materials, contributing to an increased number of buildings featuring sustainable solutions.

However, to significantly advance applications of CNF-ALG hydrogels in specific building systems, elements, and architectural products, in the future studies it will be necessary to continue developing the upscaling methods for 3D printed ambient dried membranes. It will also be paramount to further investigate the interdependencies between the geometry of the toolpath, the dimensions of the 3D printed constructs, and the shrinkage, deformation and appearance transitions affecting the final dried membrane products. Functional aspects important for building materials, such as fire resistance, mechanical performance and hydrophilic properties concerning the interaction of the material with water and vapor in humid environments will also need to be studied in connection with more specific architectural application areas and products.

In summary, this study has demonstrated that CNF-ALG hydrogel is a scalable, 3D printable, and customizable material with application potential in many lightweight architectural products. The membrane designs can be tuned using custom material deposition paths and ambient drying scenarios. This high level of control, achievable through custom design and bespoke 3D printing strategies, directly affects the aesthetic features and shape characteristics of the membranes, making them a promising option for highly personalized, multifunctional, bio-based products. The ability to adjust color, translucency, texture, porosity, and form is relevant for architectural applications and, combined with the functional properties and environmental benefits of the nanocellulose material, provides significant advantages over other lightweight building materials that have a higher ecological footprint and are based on fossil resources. Therefore, it can be concluded that CNF-ALG hydrogel is a viable alternative for decarbonized architecture, paving the way for a new generation of biodegradable building components.

Declaration of Competing Interest

The authors declare that they have no known competing financial interests or personal relationships that could have appeared to influence the work reported in this paper.

Data availability

Data will be made available on request.

Acknowledgements

This work was supported by Adlerbertska Research Foundation [grant number C 2021-1258] and Chalmers University of Technology's Area of Advance Materials Science [grant number C 2021-0037]. The Knut and Alice Wallenberg Foundation is gratefully acknowledged for funding the Wallenberg Wood Science Center. The authors would also like to recognize the contribution of Karl Åhlund, who assisted in the robotic extrusion system development.

References

[1] International Energy Agency, Global status report for buildings and construction 2019. https://www.iea.org/reports/global-status-report-for-buildings-and-construction-2019/, 2019 (accessed 1 June 2023).
[2] M. Röck, M.R. Saade, M. Balouktsi, F.N. Rasmussen, H. Birgisdottir, R. Frischknecht, G. Habert, T. Lützkendorf, A. Passer, Embodied GHG emissions of buildings: The hidden challenge for effective climate change mitigation, Appl. Energy 258 (2020), 114107, https://doi.org/10.1016/j.apenergy.2019.114107.
[3] European Commission, Delivering the European Green Deal. https://commission.europa.eu/strategy-and-policy/priorities-2019-2024/european-green-deal/delivering-european-green-deal_en/, 2019 (accessed 1 June 2023).
[4] European Commission, Statement by President von der Leyen on the occasion of the New European Bauhaus goes into the woods event. https://ec.europa.eu/commission/presscorner/detail/es/statement_22_7120/, 2022 (accessed 1 June 2023).
[5] F. Pomponi, A. Moncaster, Circular economy for the built environment: A research framework, J. Clean. Prod. 143 (2017) 710–718, https://doi.org/10.1016/j.jclepro.2016.12.055.
[6] K.M. Rahla, R. Mateus, L. Bragança, Implementing circular economy strategies in buildings: From theory to practice, Appl. Syst. Innov. 4 (2021) 26, https://doi.org/10.3390/asi4020026.
[7] R. Geyer, B. Kuczenski, T. Zink, A. Henderson, Common misconceptions about recycling, J. Ind. Ecol. 20 (2016) 1010–1017, https://doi.org/10.1111/jiec.12355.
[8] Ministry of the Environment Finland, Plastics in buildings: A study of Finnish blocks of flats and daycare centres. https://muovitiekartta.fi/wp-content/uploads/2019/03/Plastics-in-buildings-report.pdf, 2019 (accessed 1 June 2023).
[9] R.P. Babu, K. O'Connor, R. Seeram, Current progress on bio-based polymers and their future trends, Prog. Biomater. 2 (2013) 1–6, https://doi.org/10.1186/2194-0517-2-8.

[10] D. Trache, Nanocellulose as a promising sustainable material for biomedical applications, AIMS Mater. Sci. 5 (2018) 201–205, https://doi.org/10.3934/matersci.2018.2.201.
[11] D. Trache, A.F. Tarchoun, M. Derradji, T.S. Hamidon, N. Masruchin, N. Brosse, M. H. Hussin, Nanocellulose: From fundamentals to advanced applications, Front. Chem. 8 (2020) 392, https://doi.org/10.3389/fchem.2020.00392.
[12] D. Klemm, F. Kramer, S. Moritz, T. Lindström, M. Ankerfors, D. Gray, A. Dorris, Nanocelluloses: A new family of nature-based materials, Angew. Chem. Int. Ed. 50 (2011) 5438–5466, https://doi.org/10.1002/anie.201001273.
[13] E.J. Foster, R.J. Moon, U.P. Agarwal, M.J. Bortner, J. Bras, S. Camarero-Espinosa, K.J. Chan, M.J. Clift, E.D. Cranston, S.J. Eichhorn, D.M. Fox, Current characterization methods for cellulose nanomaterials, Chem. Soc. Rev. 47 (2018) 2609–2679, https://doi.org/10.1039/C6CS00895J.
[14] T.C. Mokhena, M.J. John, Cellulose nanomaterials: New generation materials for solving global issues, Cellulose 27 (2020) 1149–1194, https://doi.org/10.1007/s10570-019-02889-w.
[15] S. Naz, J.S. Ali, M. Zia, Nanocellulose isolation characterization and applications: A journey from non-remedial to biomedical claims, Bio-Des. Manuf. 2 (2019) 187–212, https://doi.org/10.1007/s42242-019-00049-4.
[16] M. Rajinipriya, M. Nagalakshmaiah, M. Robert, S. Elkoun, Importance of agricultural and industrial waste in the field of nanocellulose and recent industrial developments of wood based nanocellulose: A review, ACS Sustain. Chem. Eng. 6 (2018) 2807–2828, https://doi.org/10.1021/acssuschemeng.7b03437.
[17] R. Curvello, V.S. Raghuwanshi, G. Garnier, Engineering nanocellulose hydrogels for biomedical applications, Adv. Colloid Interface Sci. 267 (2019) 47–61, https://doi.org/10.1016/j.cis.2019.03.002.
[18] J. Mantovan, J. Pereira, B. Marim, V. Resta, G. Gil-Giraldo, S. Mali, Nanocellulose hydrogels, in: S.M. Sapuan, M.N.F. Norrrahim, R.A. Ilyas, C. Soutis (Eds.), Industrial Applications of Nanocellulose and Its Nanocomposites, Elsevier, Cambridge, 2022, pp. 263–287, https://doi.org/10.1016/B978-0-323-89909-3.00019-5.
[19] K. Markstedt, K. Håkansson, G. Toriz, P. Gatenholm, Materials from trees assembled by 3D printing: Wood tissue beyond nature limits, Appl. Mater. Today 15 (2019) 280–285, https://doi.org/10.1016/j.apmt.2019.02.005.
[20] M.K. Yazdi, V. Vatanpour, A. Taghizadeh, M. Taghizadeh, M.R. Ganjali, M. T. Munir, S. Habibzadeh, M.R. Saeb, M. Ghaedi, Hydrogel membranes: a review, Mater. Sci. Eng. C 114 (2020), 111023, https://doi.org/10.1016/j.msec.2020.111023.
[21] L. Bacakova, J. Pajorova, M. Bacakova, A. Skogberg, P. Kallio, K. Kolarova, V. Svorcik, Versatile application of nanocellulose: From industry to skin tissue engineering and wound healing, Nanomaterials 9 (2019) 164. https://doi.org/10.3390%2Fnano9020164.
[22] K. Markstedt, A. Mantas, I. Tournier, H. Martínez Ávila, D. Hagg, P. Gatenholm, 3D bioprinting human chondrocytes with nanocellulose–alginate bioink for cartilage tissue engineering applications, Biomacromolecules 16 (2015) 1489–1496, https://doi.org/10.1021/acs.biomac.5b00188.
[23] O.A. Dias, S. Konar, A.L. Leão, W. Yang, J. Tjong, M. Sain, Current state of applications of nanocellulose in flexible energy and electronic devices, Front. Chem. 8 (2020) 420, https://doi.org/10.3389/fchem.2020.00420.
[24] X. Du, Z. Zhang, W. Liu, Y. Deng, Nanocellulose-based conductive materials and their emerging applications in energy devices: A review, Nano Energy 35 (2017) 299–320, https://doi.org/10.1016/j.nanoen.2017.04.001.
[25] L. Hu, G. Zheng, J. Yao, N. Liu, B. Weil, M. Eskilsson, E. Karabulut, Z. Ruan, S. Fan, J.T. Bloking, M.D. McGehee, Transparent and conductive paper from nanocellulose fibers, Energy Environ. Sci. 6 (2013) 513–518, https://doi.org/10.1039/C2EE23635D.
[26] A. Isogai, Emerging nanocellulose technologies: Recent developments, Adv. Mater. 33 (2021) 2000630, https://doi.org/10.1002/adma.202000630.
[27] M.N. Norrrahim, N.A. Kasim, V.F. Knight, F.A. Ujang, N. Janudin, M.A. Razak, N. A. Shah, S.A. Noor, S.H. Jamal, K.K. Ong, W.M. Yunus, Nanocellulose: The next super versatile material for the military, Mater. Adv. 2 (2021) 1485–1506, https://doi.org/10.1039/D0MA01011A.
[28] C. Aulin, M. Gällstedt, T. Lindström, Oxygen and oil barrier properties of microfibrillated cellulose films and coatings, Cellulose 17 (2010) 559–574, https://doi.org/10.1007/s10570-009-9393-y.
[29] H.M. Azeredo, M.F. Rosa, L.H. Mattoso, Nanocellulose in bio-based food packaging applications, Ind. Crops Prod. 97 (2017) 664–671, https://doi.org/10.1016/j.indcrop.2016.03.013.
[30] K. Shanmugam, H. Doosthosseini, S. Varanasi, G. Garnier, W. Batchelor, Nanocellulose films as air and water vapour barriers: A recyclable and biodegradable alternative to polyolefin packaging, Sustain. Mater. Technol. 22 (2019) e00115.
[31] A. Cataldi, C.E. Corcione, M. Frigione, A. Pegoretti, Photocurable resin/nanocellulose composite coatings for wood protection, Prog. Org. Coat. 106 (2017) 128–136, https://doi.org/10.1016/j.porgcoat.2017.01.019.
[32] C. Cianci, D. Chelazzi, G. Poggi, F. Modi, R. Giorgi, M. Laurati, Hybrid fibroin-nanocellulose composites for the consolidation of aged and historical silk, Colloids Surf. A: Physicochem. Eng. Asp. 634 (2022), 127944, https://doi.org/10.1016/j.colsurfa.2021.127944.
[33] A. Fornari, M. Rossi, D. Rocco, L. Mattiello, A review of applications of nanocellulose to preserve and protect cultural heritage wood, paintings, and historical papers, Appl. Sci. 12 (2022) 12846, https://doi.org/10.3390/app122412846.
[34] R. Rudin, M.A. Zboinska, S. Sämfors, P. Gatenholm, RePrint: A digital workflow for aesthetically retrofitting deteriorated architectural elements with new biomaterial finishes, in: M. Akbarzadeh, D. Aviv, H. Jamelle, R. Stuart-Smith (Eds.), Hybrids & Haecceities: Proceedings of the 42nd Annual Conference of the Association for Computer Aided Design in Architecture, 2022, pp. 336–345.
[35] C. Zinge, B. Kandasubramanian, Nanocellulose based biodegradable polymers, Eur. Polym. J. 133 (2020), 109758, https://doi.org/10.1016/j.eurpolymj.2020.109758.
[36] M. Adaloudis, J.B. Roca, Sustainability tradeoffs in the adoption of 3D concrete printing in the construction industry, J. Clean. Prod. 307 (2021), 127201, https://doi.org/10.1016/j.jclepro.2021.127201.
[37] R. Guamán-Rivera, A. Martínez-Rocamora, R. García-Alvarado, C. Muñoz-Sanguinetti, L.F. González-Böhme, F. Auat-Cheein, Recent developments and challenges of 3D-printed construction: A review of research fronts, Buildings 12 (2022) 229, https://doi.org/10.3390/buildings12020229.
[38] L.A. Verhoef, B.W. Budde, C. Chockalingam, B.G. Nodar, A.J. van Wijk, The effect of additive manufacturing on global energy demand: an assessment using a bottom-up approach, Energy Policy 112 (2018) 349–360, https://doi.org/10.1016/j.enpol.2017.10.034.
[39] S. Guo, T.M. Choi, S.H. Chung, Self-design fun: should 3D printing be employed in mass customization operations, Eur. J. Oper. Res. 299 (2022) 883–897, https://doi.org/10.1016/j.ejor.2021.07.009.
[40] I.J. Petrick, T.W. Simpson, 3D printing disrupts manufacturing: How economies of one create new rules of competition, Res. Technol. Manag. 56 (2013) 12–16, https://doi.org/10.5437/08956308X5606193.
[41] N. Shahrubudin, T.C. Lee, R.J. Ramlan, An overview on 3D printing technology: Technological, materials, and applications, Procedia Manuf. 35 (2019) 1286–1296, https://doi.org/10.1016/j.promfg.2019.06.089.
[42] X. Bi, R. Huang, 3D printing of natural fiber and composites: a state-of-the-art review, Mat. Des. 222 (2022), 111065, https://doi.org/10.1016/j.matdes.2022.111065.
[43] S. Malik, J. Hagopian, S. Mohite, C. Lintong, L. Stoffels, S. Giannakopoulos, R. Beckett, C. Leung, J. Ruiz, M. Cruz, B. Parker, Robotic extrusion of algae-laden hydrogels for large-scale applications, Global Chall. 4 (2020) 1900064, https://doi.org/10.1002/gch2.201900064.
[44] J. Duro-Royo, L. Mogas-Soldevila, N. Oxman, Flow-based fabrication: An integrated computational workflow for design and digital additive manufacturing of multifunctional heterogeneously structured objects, Comput. Aided Des. 69 (2015) 143–154, https://doi.org/10.1016/j.cad.2015.05.005.
[45] L. Mogas-Soldevila, J. Duro-Royo, N. Oxman, Water-based robotic fabrication: Large-scale additive manufacturing of functionally graded hydrogel composites via multichamber extrusion, 3D Print, Addit. Manuf. 1 (2014) 141–151, https://doi.org/10.1089/3dp.2014.0014.
[46] L. Mogas-Soldevila, N. Oxman, Water-based engineering & fabrication: Large-scale additive manufacturing of biomaterials, Mater. Res. Soc. Symp. Proc. 1800 (2015) 7, https://doi.org/10.1557/opl.2015.659.
[47] L. Mogas-Soldevila, G. Matzeu, M.L. Presti, F.G. Omenetto, Additively manufactured leather-like silk protein materials, Mater. Des. 203 (2021), 109631, https://doi.org/10.1016/j.matdes.2021.109631.
[48] X. Zhang, M. Morits, C. Jonkergouw, A. Ora, J.J. Valle-Delgado, M. Farooq, R. Ajdary, S. Huan, M. Linder, O. Rojas, M.H. Sipponen, M. Österberg, Three-dimensional printed cell culture model based on spherical colloidal lignin particles and cellulose nanofibril-alginate hydrogel, Biomacromolecules 21 (2020) 1875–1885, https://doi.org/10.1021/acs.biomac.9b01745.
[49] R. Olmos-Juste, B. Alonso-Lerma, R. Pérez-Jiménez, N. Gabilondo, A. Eceiza, 3D printed alginate-cellulose nanofibers based patches for local curcumin administration, Carbohydr. Polym. 264 (2021), 118026, https://doi.org/10.1016/j.carbpol.2021.118026.
[50] M.S. Peresin, J. Vartiainen, V. Kunnari, T. Kaljunen, T. Tammelin, P. Qvintus, Large-scale nanofibrillated cellulose film: An overview on its production, properties, and potential applications, in: Book of abstracts of the 4th International Conference of Pulping, Papermaking and Biotechnology ICPPB'12, Nanjing, China, 2012, pp. 891–895.
[51] K. Shanmugam, S. Varanasi, G. Garnier, W. Batchelor, Rapid preparation of smooth nanocellulose films using spray coating, Cellulose 24 (2017) 2669–2676, https://doi.org/10.1007/s10570-017-1328-4.
[52] Q. Wang, Q. Yao, J. Liu, J. Sun, Q. Zhu, H. Chen, Processing nanocellulose to bulk materials: a review, Cellulose 26 (2019) 7585–7617, https://doi.org/10.1007/s10570-019-02642-3.
[53] H. Nadeem, M. Dehghani, G. Garnier, W. Batchelor, Life cycle assessment of cellulose nanofibril films via spray deposition and vacuum filtration pathways for small scale production, J. Clean. Prod. 342 (2022), 130890, https://doi.org/10.1016/j.jclepro.2022.130890.
[54] Q. Chen, C.J. Brett, A. Chumakov, M. Gensch, M. Schwartzkopf, V. Körstgens, L. D. Söderberg, A. Plech, P. Zhang, P. Müller-Buschbaum, S.V. Roth, Layer-by-layer spray-coating of cellulose nanofibrils and silver nanoparticles for hydrophilic interfaces, ACS Appl. Nano Mater. 4 (2021) 503–513, https://doi.org/10.1021/acsanm.0c02819.
[55] A. Hajian, Z. Wang, L.A. Berglund, M.M. Hamedi, Cellulose nanopaper with monolithically integrated conductive micropatterns, Adv. Electron. Mater. 5 (2019) 1800924, https://doi.org/10.1002/aelm.201800924.
[56] H. Nadeem, M. Naseri, K. Shanmugam, C. Browne, G. Garnier, W. Batchelor, Impact of heat drying on the physical and environmental characteristics of the

nanocellulose-based films produced via spray deposition technique, Cellulose 27 (2020) 10225–10239, https://doi.org/10.1007/s10570-020-03473-3.
[57] K.M. Håkansson, I.C. Henriksson, C. de la Peña Vázquez, V. Kuzmenko, K. Markstedt, P. Enoksson, P. Gatenholm, Solidification of 3D printed nanofibril hydrogels into functional 3D cellulose structures, Adv. Mater. Technol. 1 (2016) 1600096, https://doi.org/10.1002/admt.201600096.
[58] M.W. Schwarz, W.B. Cowan, J.C. Beatty, An experimental comparison of RGB, YIQ, LAB, HSV, and opponent color models, ACM Trans. Graph. 6 (1987) 123–158, https://doi.org/10.1145/31336.31338.